

# Observations of Flow and Turbulence in the Nocturnal Boundary Layer over a Slope

P. MONTI

*Dipartimento di Idraulica Trasporti e Strade, Università degli Studi di Roma, La Sapienza, Rome, Italy*

H. J. S. FERNANDO, M. PRINCEVAC, AND W. C. CHAN

*Department of Mechanical and Aerospace Engineering, Arizona State University, Tempe, Arizona*

T. A. KOWALEWSKI

*IPPT PAN, Polish Academy of Sciences, Warsaw, Poland*

E. R. PARDYJAK\*

*Los Alamos National Laboratory, Los Alamos, New Mexico*

(Manuscript received 10 September 2001, in final form 22 February 2002)

## ABSTRACT

Measurements were conducted on an eastern slope of the Salt Lake Basin (SLB) as a part of the Vertical Transport and Mixing Experiment (VTMX) conducted in October 2000. Of interest was the nocturnal boundary layer on a slope (in particular, katabatic flows) in the absence of significant synoptic influence. Extensive measurements of mean flow, turbulence, temperature, and solar radiation were made, from which circulation patterns on the slope and the nature of stratified turbulence in katabatic winds were inferred. The results show that near the surface (<25–50 m) the nocturnal flow is highly stratified and directed downslope, but at higher levels winds strongly vary in magnitude and direction with height and time, implying the domination of upper levels by air intrusions. These intrusions may peel off from different slopes surrounding the SLB, have different densities, and flow at their equilibrium density levels. The turbulence was generally weak and continuous, but sudden increases of turbulence levels were detected as the mean gradient Richardson number ( $\overline{Ri_g}$ ) dropped to about unity. With a short timescale  $\overline{Ri_g}$  fluctuated on the order of a few tens of seconds while modulating with a longer (along-slope internal waves sloshing) timescale of about half an hour. The mixing efficiency (or the flux Richardson number) of the flow was found to be a strong function of  $\overline{Ri_g}$ , similar to that found in laboratory experiments with inhomogeneous stratified shear flows. The eddy diffusivities of momentum and heat were evaluated, and they showed a systematic variation with  $\overline{Ri_g}$  when scaled with the shear length scale and the rms vertical velocity of turbulence.

## 1. Introduction

Slope flows play an important role in the diurnal circulation of complex terrain regions (areas replete with mountains, valleys, and other topographic features). These flows, caused by the thermal forcing on topographic surfaces, belong to the well-known class of winds known as “thermal circulation.” Thermal circulations span a range of scales, from a few kilometers

scale such as flow over a simple slope to meso- $\beta$ -scale diurnal circulation systems with horizontal scales on the order of 100 km or more (Bossert and Cotton 1994). Slope flows are produced by the horizontal temperature difference between air adjacent to a mountain slope and the ambient air at the same altitude over the center of the valley; heating during the day and radiative cooling at night near the surface contribute to this temperature differential [for reviews, see Scorer (1978), Simpson (1999), and Whiteman (2000)]. The daytime flow is typically upslope (also known as anabatic flow), whereas the nighttime flow is downslope (katabatic or drainage winds). Slope currents are characterized by sustained wind speeds, typically 1–5 m s<sup>-1</sup>, and the transition between slope flows in the early morning and in the late afternoon is characterized by periods of very low winds <0.5 m s<sup>-1</sup> (Papadopoulos and Helmis

---

\* Current affiliation: Department of Mechanical Engineering, University of Utah, Salt Lake City, Utah.

---

Corresponding author address: Prof. H. J. S. Fernando, Environmental Fluid Dynamics Program, Department of Mechanical and Aerospace Engineering, Arizona State University, Tempe, AZ 85287-9809.  
E-mail: j.fernando@asu.edu

1999). Associated with such low winds are the reduced dispersion and transport that contribute to serious air pollution problems, which are known to plague many complex terrain airsheds (Whiteman 1990, 2000).

Thermal circulation in complex terrain has been studied by many investigators, principally using field experiments. The field studies have been conducted under a variety of conditions ranging from such extreme environments as Antarctica [e.g., Lied's (1964) observations of "hydraulic jumps" in strong katabatic winds on the order of  $20 \text{ m s}^{-1}$ ] to calmer conditions prevailing over gentle slopes in the absence of synoptic winds (Mahrt 1990). Owing to the natural variability, however, it is difficult to have control over field conditions, and hence datasets so obtained often do not span wide parameter ranges nor can they be used effectively for process studies. Theoretical (Prandtl 1952; McNider and Pielke 1981; Doran and Horst 1983; Arritt and Pielke 1986; Doran et al. 1990), numerical (Yamada 1981; Tripoli and Cotton 1989; Bossert and Cotton 1994), and laboratory-scale (Meroney 1990; Snyder et al. 1990) studies also have been reported to investigate slope flows, which have their own merits and drawbacks. For example, due to the complexity of the problem, theoretical studies employ idealized flow configurations whereas parameterization of small-scale stably stratified turbulence is the bane for numerical modeling. Matching similarity parameters between laboratory models and natural conditions also remains a serious challenge (Cermak 1996).

Based on previous studies, certain general characteristics of slope flows can be identified. Owing to the differences in the nature of forcing, the structure and dynamics of anabatic and katabatic winds differ significantly. Figures 1a–c present schematics of anabatic, evening transitional, and katabatic flows on a simple slope. During the day, the incoming shortwave radiation  $R_i$  is absorbed by the ground as well as by the air layer near the ground, which provides forcing for the anabatic flow and thermal convection therein. The sensible heat flux  $Q_h (> 0)$  near the ground transmitted to the air layer aloft is on the order of  $R_i$ , the outgoing longwave radiation during the day being smaller. The flow near the ground is dominated by the mechanical (shear) turbulence (specified by the friction velocity  $u_*$ ). Beyond a distance on the order of the Monin–Obukhov length scale  $L_*$  above the surface, convective turbulence overshadows the frictional influence. Here  $L_*$  is defined as

$$L_* = \frac{u_*^3}{\kappa q_0}, \quad (1.1)$$

where  $\kappa$  is the von Kármán constant and  $q_0 = \alpha g Q_h / \rho c_p$  is the surface buoyancy flux defined in terms of physical constants; here  $\alpha \cong \frac{1}{\bar{\theta}}$  is the thermal expansion coefficient,  $g$  the gravitational acceleration,  $\bar{\theta}$  the mean potential temperature (virtual potential temperature, in the case of humid atmosphere),  $\rho$  the density,

and  $c_p$  the specific heat. The height of the anabatic layer  $h$  and its time evolution depend, inter alia, on the nature, magnitude, and duration of thermal forcing and the static stability of the background stratification expressed in terms of the background potential temperature gradient, namely,

$$N^2 = \frac{g}{\bar{\theta}_r} \frac{d\bar{\theta}}{dz}, \quad (1.2)$$

where  $\bar{\theta}_r$  is a reference temperature,  $N$  the buoyancy frequency, and  $z$  is the vertical coordinate (see Fig. 1a for the coordinate systems used). Laboratory experiments (Fernando et al. 2000, 2001) show that partially mixed fluid at the edge of the upslope flow may peel off in the form of approximately horizontal intrusions ("detrainment") that propagate along their neutrally buoyant level. For smaller slopes, the characteristic velocity in the convective layer can be considered as the Deardorff (1970) scale,  $w_* = (q_0 h)^{1/3}$ , but for larger slopes this may not be true (Deardorff and Willis 1987). Because of effective momentum and property (e.g., heat) transports in the vertical direction, the velocity and property gradients in anabatic flows at heights well beyond  $L_*$  are small.

Cooling of the ground and adjacent air layer during the evening causes the upslope flow to reverse. Simplified theoretical models (Hunt et al. 2002, manuscript submitted to *J. Atmos. Sci.*) indicate that the transition from the upslope to downslope flow occurs via the formation of a stagnant frontal region, as depicted in Fig. 1b. While flowing upslope, air parcels at various heights ( $z$ ) cool and gradually decrease their buoyancy; they stagnate at a certain distance from the origin where the upslope inertia of fluid parcels are too feeble to overcome along-slope negative buoyancy forces. Note that the upper air layers have higher inertia vis-à-vis the lower levels (due to the very nature of the velocity profile) and hence the stagnation line appears as a front. The ensuing flow topology facilitates overturning (and rapid mixing) motions on the upslope side of the front (due to the rise of dense fluid parcels). Relatively warmer air parcels from immediately above the ground may follow the frontal boundary and mix with overturning motions as shown. Laboratory observations confirm the efficacy of this transition mechanism (Fernando et al. 2000) and show that this frontal region is nonstationary and migrates downslope, causing the cool air layer behind the front to drain, initiating the katabatic flow. The overturning frontal structure may take the form of gravity current heads observed in laboratory experiments (Simpson 1999). Figure 1c depicts the flow situation during the establishment of the katabatic flow. Note that, aloft the ensuing katabatic flow, the upslope flow can persist for some time due to the inertia of air parcels at greater heights.

Katabatic flows (Fig. 1c) differ much from their anabatic counterpart in that the air layer within the former

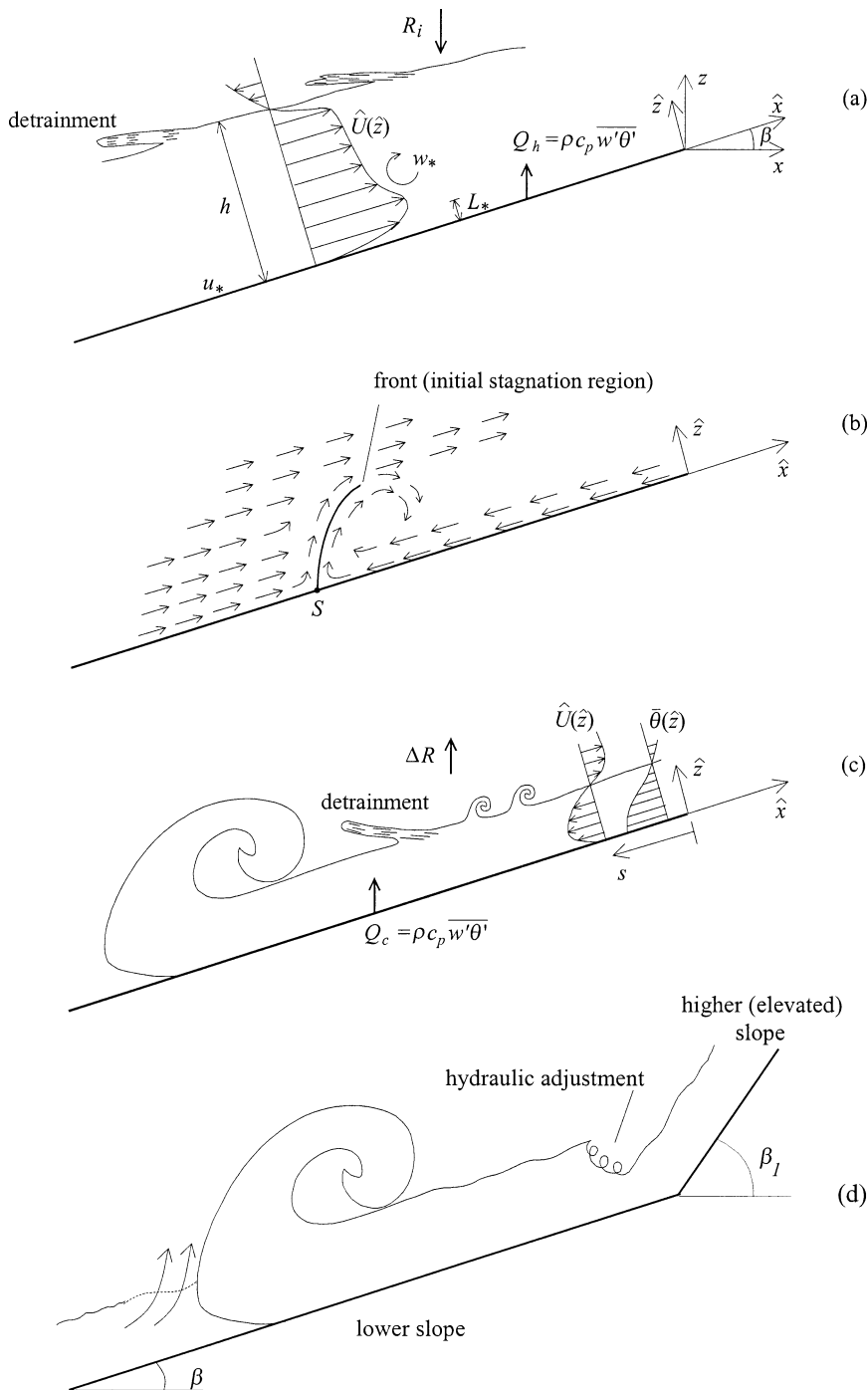


FIG. 1. Schematic of slope flows: (a) upslope (anabatic) current, showing useful scales, velocity profile, and the detrainment phenomenon; (b) transition from upslope to downslope flow (S indicates the stagnation region); (c) downslope flow, including the downslope propagating frontal region; and (d) evolution of katabatic flow over a discontinuous slope.

is stably stratified. Turbulence in such stable flows are inhibited (Hunt 1985; Hunt et al. 1985; Fernando 1991), thus retarding the vertical exchange of momentum and other properties. Therefore, katabatic flows can sustain large velocity shears between different vertical layers.

The presence of layers of different densities and velocities stacked one above the other is particularly striking in complex terrain air basins, where katabatic flows from slopes of different orientation can intrude upon the basin, one layer flowing above the other in different di-

rections at their neutrally density levels (Fernando et al. 2001).

Most of the analytical and numerical work on slope flows have been performed with “ideal” katabatic flows, those that are driven solely by radiative cooling on simple uniform slopes in the absence of background winds (as in Fig. 1c). The modeling strategies have been either to (i) consider detail vertical structure of the flow, which is assumed to be invariant in the streamwise direction (Prandtl 1952) or modifications thereof (Doran and Horst 1983; Garrett 1983); (ii) use depth-averaged equations, where downslope variations are considered (Ellison and Turner 1959; Manins and Sawford 1979a; Briggs 1981); or (iii) employ full 2D or 3D numerical simulations, where both spatial and temperature evolution are predicted (Nappo and Rao 1987; Yamada 1981). The simplicity of ideal katabatic flows facilitates the eduction of processes that contribute to natural flows, in addition to being conducive for simple analytical solutions. For example, for  $N = 0$ , the Manins and Sawford (1979a) model, together with Briggs’ (1981) semiempirical relationship for the entrainment coefficient  $E = 0.05(\sin\beta)^{2/3}$ , yields integral scales of katabatic layer depth  $h_t$ , velocity  $U_t$ , and buoyancy  $\Delta b_t$ , as (Nappo and Rao 1987)

$$h_t \approx 0.073(\sin\beta)^{2/3}s, \quad (1.3a)$$

$$U_t \approx 2.5(\sin\beta)^{2/9}B_0^{1/3}s^{1/3}, \quad \text{and} \quad (1.3b)$$

$$\Delta b_t \approx 8.2(\sin\beta)^{-8/9}B_0^{2/3}s^{-1/3}, \quad (1.3c)$$

where  $\beta$  is the slope angle,  $B_0$  the stabilizing buoyancy flux driving the flow, and  $s$  the along-slope distance measured downward ( $-\hat{x}$  direction). Field verification of (1.3) and the like is hampered by the complexity of natural katabatic flows, the configurations of which are often far removed from that assumed in modeling. Possible complications include flow convergence from tributaries and sidewalls, presence of ambient winds, and change (discontinuity) of slope along the flow path (e.g., Fig. 1d). Terrain with simple deviations from the ideal configuration can lead to flow convergence and hence cross flows (Manins and Sawford 1979b).

Discontinuity in slopes may lead to interesting new phenomena. Flows from higher elevation, steeper slopes can drain down to gentler slopes of lower elevation, overrunning the existing katabatic flows. The interaction between air flows originating at disparate elevations are discussed in Hunt et al. (2002, manuscript submitted to *J. Atmos. Sci.*). Figure 1d illustrates a flow situation with a slope discontinuity. According to Manins and Sawford (1979a), hydraulics of katabatic flows on a simple slope depends on  $CRi$ , where  $C \approx 0.11$  is a constant and  $Ri = 0.055(\Delta b_t h_t / U_t^2)(\sin\beta)^{-1/3}$  is a bulk Richardson number. When  $CRi < 1$ , the flow is supercritical in that all disturbances are swept downstream, barring the propagation of information upstream. Based on (1.3), therefore, all slopes with  $\sin\beta > 6 \times 10^{-4}$  (or  $\beta > 0.035^\circ$ )

favor supercritical flows. Flows originating at higher (elevated) slopes with steeper gradients are more liable for supercriticality, and hence adjustments at the slope discontinuity are expected to be associated with a hydraulic jump. As shown in Fig. 1d, the passage of a drainage layer from a higher to a lower slope can lead to an increase of the layer thickness through a hydraulic jump, since larger  $\beta$  supports larger velocities and flow rates. The initial spate on the lower slope is expected to be associated with a gravity current front that outstrips the existing shallow katabatic layer. Mixing of the two air masses in the frontal region may lead to local cooling (due to the rising of cold fluid from the surface layer), followed by warming (due to overturning of warmer air entrainment from above the front) events. At longer times, the flow is expected to adjust to a quasi steady state.

Although the stable stratification inhibits turbulent motions in katabatic flows, the generation of large velocity shears causes the flow to be unstable and break down into turbulence, at least intermittently. On the proviso of linear analysis of Miles (1961) and Howard (1961), the gradient Richardson number  $Ri_g$  is used as an indicator of the flow stability, namely,

$$Ri_g = \frac{N^2}{\left[\frac{\partial \tilde{V}}{\partial z}\right]^2} = \frac{N^2}{\left(\frac{\partial U}{\partial z}\right)^2 + \left(\frac{\partial V}{\partial z}\right)^2}, \quad (1.4)$$

where the mean velocity vector is expressed as  $\tilde{V} = (U, V, W)$ ,  $U, V$  being the horizontal ( $x, y$ ) velocities and  $W$  the (small) vertical ( $z$ ) velocity. The Miles–Howard stability criterion was developed for unbounded stratified parallel shear flows having a velocity profile  $U(z)$ , where it was shown that the flow can become unstable when  $Ri_g = N^2/(dU/dz)^2$  drops below a critical values of  $Ri_{gc} = 0.25$ . This critical value can be much different from 0.25 for nonlinear disturbances (Miles 1987). According to the experiments of Strang and Fernando (2001a,b) conducted with a parallel stratified shear flow having hyperbolic tangent velocity and density profiles, strong mixing events can persist up to  $Ri_g \approx 1$  or even beyond. For  $Ri_g < 1$ , the major mixing mechanism was the Kelvin–Helmholtz (K–H) instability. Nonlinear waves tend to generate and resonate with K–H billows when  $Ri_g \sim 1$ ,<sup>1</sup> thus producing the most efficient turbulent mixing. At still larger values of  $Ri_g$ , the K–H billowing and wave motions subside, paving the way to less intense Hölböe waves. The laboratory experiments of Baines (2001) show that these types of mixing mechanisms are also prevalent at the highly sheared edges of gravity currents flowing down the slopes (which have similarities to katabatic flows). It was shown that locally mixed fluid produced by these in-

<sup>1</sup> Here  $\sim$  is used to denote approximate equality within  $\pm 25\%$  of the value indicated.

stabilities collapse to form intrusions into the background stratification (detrainment). In the case of katabatic flows, strong mixing events are possible at the edges of the current (Mahrt et al. 2001) as well as within the current itself due to internal shear (Hootman and Blumen 1983; Blumen et al. 2001).

Indeed, a katabatic flow is a high Reynolds number inhomogeneous stratified shear flow that is amenable to extensive measurements, using which various hypotheses and theories on stratified turbulence can be tested. Instabilities and mixing events occurring in such flows are of profound importance in understanding contaminant dispersion in the lower atmosphere (Nappo 1991; Pardyjak et al. 1999) and for the development and improvement of forecasting models. It has been particularly noted that the performance of certain mesoscale atmospheric models are poor during transition and stably stratified periods, which has been attributed to the drawbacks of available turbulent closure models (e.g., Melas et al. 1995; Poulos and Bossert 1995).

The present work was motivated by the belief that katabatic flows can provide useful information on stably stratified shear flows at high Reynolds numbers that have general applicability to atmospheric and oceanic shear flows. After the evening transition is completed, a slowly varying stratified shear (katabatic) flow is established and the radiation divergence over the thickness of the katabatic layer  $\Delta R$  causes intense cooling of the flow (Fig. 1c). Cool air near the ground also causes a sensible heat flux  $Q_c$  into the ground, thus realizing a net buoyancy flux of

$$B_0 = \frac{g}{\rho c_p \theta} (\Delta R - Q_c) \quad (1.5)$$

that drives the katabatic flow (Manins and Sawford 1979a; Nappo and Rao 1987). Cooling leads to continuous variation (generally an increase) of the mean gradient Richardson number  $\overline{Ri}_g$  of the flow over the night, allowing investigations into the nature of stratified shear flows covering a range of  $\overline{Ri}_g$ . Note that the flow properties ought to be dependent on large-scale forcing parameters of the katabatic layer, especially the length scales (e.g., the shear length scale  $L_s = \sigma_w / |d\tilde{V}/dz|$ ) and timescales  $T_s$  of shear that are heavily site dependent. However, turbulence generated by shear instabilities is vertically constrained by the buoyancy length scale  $L_b = \sigma_w / N$ , where  $\sigma_w$  is the rms velocity of turbulence (Hunt 1985; Pearson et al. 1983), the corresponding timescale being  $N^{-1}$ . One may expect the resulting stratified turbulence to be sheltered by the forcing scales as far as  $T_s \gg N^{-1}$  (which is usually satisfied) and when  $L_s > L_b$ . Using conventional scaling for the turbulent kinetic energy (TKE) dissipation  $\varepsilon \sim (\sigma_w^2)^{3/2} / L_b$  for the case  $L_s > L_b$  (Fernando and Hunt 1996), we expect stratified turbulence to show behavior independent of forcing scales when  $N^2 / |d\tilde{V}/dz|^2 > 1$  or  $\overline{Ri}_g > 1$ . Therefore, under strong stably stratified conditions,

results obtained from katabatic flows are expected to have universal properties determined by local conditions (provided that the internal gravity wave radiation does not affect local balances). Nieuwstadt (1984) has also argued that stable atmospheric boundary layers reach a state governed by local parameters (also see Mahrt 1982 for similarity considerations for slope flows).

We have employed nocturnal (katabatic flow) measurements taken during the Vertical Transport and Mixing Experiment (VTMX) conducted during October 2000 in Salt Lake City, Utah, to study turbulence and mixing in stratified shear flows. This field campaign was carried out under the sponsorship of the Atmospheric Sciences Program of the Department of Energy to study the transport and mixing processes in complex terrain under stable conditions. Details of the field campaign are given in Doran et al. (2002). Nine national laboratories and two universities participated in the experiment, including our group from Arizona State University (ASU). The site, instrumentation, and experimental procedure used for the study are described in section 2. Gross characteristics of up- and downslope flows (both near the ground and elevated levels) together with analysis of the main turbulent parameters (e.g., rms velocities, momentum, and heat fluxes) are reported in section 3a. Internal gravity waves and their interactions with both the mean flow and the turbulence are discussed in section 3b, while the investigations of the mixing efficiency and eddy diffusivities under stable conditions are presented in sections 3c and 3d, respectively. Conclusions are given in section 4.

## 2. The site and the instrumentation

The Salt Lake City (SLC) metropolitan area is located in a wide valley  $\sim 1400$  m above mean sea level (MSL). The valley (Fig. 2a) is about 30 km wide (along the east–west direction) and 50 km long (north–south direction) and is surrounded by elevated mountains (up to 3000 m above MSL). The southern shoreline of the Great Salt Lake is the northwestern border of the valley. The basin-shaped topography of the SLC metropolis makes it prone to significant air pollution problems, especially when the synoptic winds are absent. Our observation site was located in the northeastern side of the valley, in a grassy open area (aerodynamic roughness length  $\sim 0.1$  m), adjoining the Mount Olivet Cemetery (ASU Cemetery Site, hereafter ACS), having a gentle slope ( $\sim 0.07$ , i.e.,  $4^\circ$ ). Because the measurements were made away from buildings and trees, the data can be considered as free from the immediate effects of obstacle wakes. The fetch was fairly uniform for 100 m uphill and 80 m downhill distances. The closest uphill feature was the Utah National Guard's building (10 m high), but it was not in the direct downslope path of the flow through the measurement station. The closest downslope feature was a mild drop in slope to accommodate a football stadium and a school with building height of

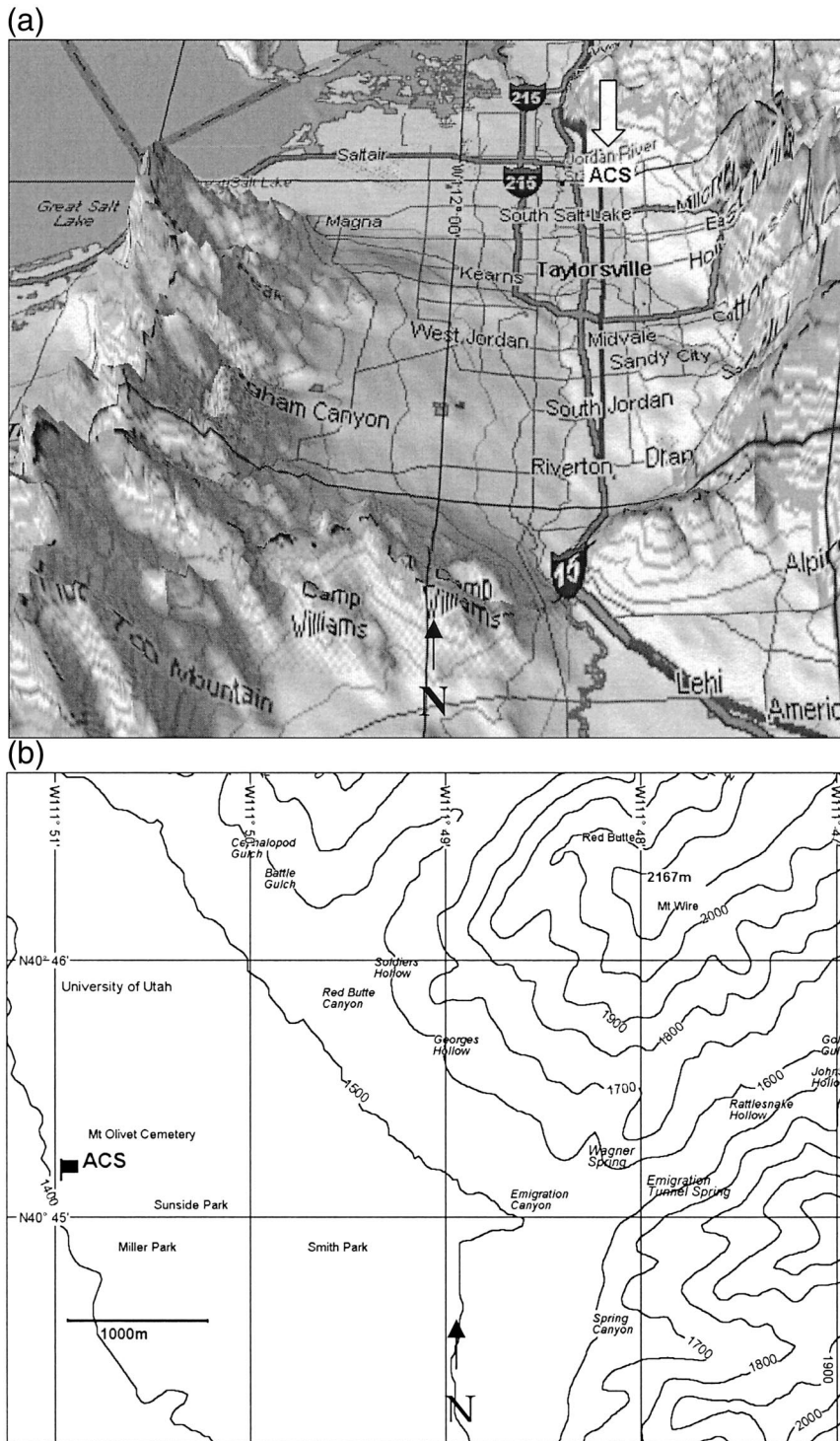


FIG. 2. (a) Perspective view of the Salt Lake Basin. The ASU site (ACS) is located at the east–north side in the vicinity of the Wasatch Mountain range. Distance between the map grid lines is 21.1 km, N shows the north direction. (b) Topographical map surrounding the experimental site. The scale of the map is shown. Downtown Salt Lake City is about 4 km west of ACS. The separation between elevation contours are 100 m.

approximately 15 m. On a much larger ( $\sim$  km) scale, the major topographic perturbation was provided by Wasatch Mountain range abutting the gentle slope; see an enlarged map of the staging area in Fig. 2b. Estimates show that the urban heat island associated with Salt Lake City and the lake breeze of the Salt Lake (which reaches the city in the early evening) do not significantly affect the nocturnal winds at ACS.

The meteorological instruments deployed by the ASU group consisted of a 14-m mast equipped with two 3-cup anemometers (Met One Instruments, Inc., starting speed  $0.5 \text{ m s}^{-1}$ ; accuracy  $\pm 1.5\%$ ) mounted 2.0 and 7.3 m AGL; two thermistors placed at 1.8 and 6.9 m AGL; an upward-facing spectral pyranometer [Eppley Precision Spectral Pyranometer (Model PSP); sensitivity  $9 \mu\text{V}(\text{W m}^{-2})^{-1}$ , response time 1 s]; and a downward-facing pyrgeometer [Eppley Precision Infrared Radiometer (Model PIR); sensitivity  $4 \mu\text{V}(\text{W m}^{-2})^{-1}$ , response time 2 s]. Both radiation instruments were located at 3.0 m AGL, enabling the measurement of incoming shortwave radiation and outgoing longwave radiation, respectively. A datalogger provided computation and storage of 5-min-averaged air temperature, wind speed, and radiation. Two ultrasonic fast-response anemometers–thermometers (Applied Technologies, Inc., and Metek GmbH) placed at 4.5 and 13.86 m AGL were used to measure the velocity components ( $U$  positive along the W–E direction,  $V$  positive along the S–N direction and vertical component  $W$  positive when directed upward; resolution and accuracy  $-0.01$  and  $\pm 0.05 \text{ m s}^{-1}$ ) and air temperature  $T$  (resolution and accuracy:  $0.01^\circ\text{C}$  and  $\pm 0.05^\circ\text{C}$ ) at 10 Hz.

In order to analyze the vertical structure of the lower atmosphere, two tethered balloons (Atmospheric Research, Inc., TSB-9,  $9 \text{ m}^3$  balloon), each carrying four tethersondes (TMT-5A-SP), were used to measure the air temperature, relative humidity, pressure, wind speed, and wind direction. The resolution and accuracy of these measurements are as follows: temperature ( $0.01^\circ\text{C}$ ,  $\pm 3\%$ ), humidity ( $0.01\%$ ,  $\pm 3\%$ ), pressure ( $0.01 \text{ mb}$ ,  $\pm 1 \text{ mb}$ ), wind speed ( $0.1 \text{ m s}^{-1}$ ,  $\pm 0.5 \text{ m s}^{-1}$ ), and wind direction (measured clockwise,  $N$  taken as  $0^\circ$ ,  $0.1^\circ$ ,  $\pm 10^\circ$ ). Simultaneous measurements of ground-level aerosols and vertical aerosol profiles were also made, which are described in Alexandrova et al. (2002, manuscript submitted to *J. Environ. Quality*). Because of the Federal Aviation Administration traffic control limitations, the maximum height of balloon flights was set at 500 m AGL.

The field campaign at ACS covered the period 1–18 October 2000 (Julian days, hereinafter Jday, from 274 to 292, taking 00.00 of 1 January as Jday 00.00). This period was characterized by 7 days of mild weather conditions (i.e., clear skies and light synoptic winds), during which several intense observational periods (IOPs) took place from 1700 LST (2300 UTC) to 1000 LST (1600 UTC) of the following day, except that the last three IOPs were extended until 1300 LST (1900

UTC) to capture delayed transition (LST corresponds to mountain standard time). These extended observations also allowed detailed investigations of aerosol transport by the daytime upslope flow.

### 3. Results and discussion

#### a. Observations in slope winds

Owing to weak synoptic winds (generally  $< 5 \text{ m s}^{-1}$ ) and strong solar insolation, the first 5 days of the 18-day campaign were conducive for the development of slope flows. Therefore, the period 1–5 October (Jdays 274–278) was chosen for a case study to be described below.

The main meteorological quantities recorded at 13.86 m by the upper sonic anemometer and the radiometers are presented in Figs. 3 and 4. The 5-min averages of incoming shortwave radiation and outgoing longwave radiation, air temperature, wind speed parallel to the slope ( $[\hat{U}^2 + \hat{V}^2]^{1/2}$ ), wind direction (Figs. 3a–d, respectively), and the vertical ( $z$ ) wind component (Fig. 4) are shown. The outgoing longwave radiation peaked ( $\sim 600 \text{ W m}^{-2}$ ) at the same time as the maximum ground temperature, somewhat lagging behind the maximum incoming shortwave radiation ( $\sim -750 \text{ W m}^{-2}$  at 1400 LST). Conversely, the minimum outgoing radiation typically occurred at sunrise. It is easy to note that, except for the case of wind speed that showed quite distinct variability (Fig. 3c), a well-defined daily periodic behavior is evident in all variables. The temperature (Fig. 3b) varied approximately sinusoidally, with a maximal excursion of  $\sim 5^\circ\text{C}$  around the daily average. The temperature maxima were observed  $\sim 4 \text{ h}$  after the occurrence of the highest solar radiation, while temperature minima typically took place about 15 min after the sunrise ( $\sim 0725 \text{ LST}$ ). Figure 3b also depicts the air temperature measured by sonic anemometer placed at 4.5 m (dashed line). The lower nocturnal values recorded therein are a result of the stable stratification developed near the ground due to intense net radiative cooling, with temperature gradients being  $(dT/dz) \sim 0.2^\circ\text{C m}^{-1}$ , corresponding to a buoyancy frequency of  $N \sim 0.08 \text{ rad s}^{-1}$ . During the daytime, due to surface heating, a negative vertical temperature gradient is formed.

Due to the orientation of the site, with E–W nearly parallel to the slope (Fig. 2), both easterly nighttime ( $\sim 90^\circ$ , downslope at ACS) and westerly daytime ( $\sim 270^\circ$ , upslope) winds recurred for all 5 days (Fig. 3d). Both slope currents were accompanied by sustained wind speeds ( $\sim 4 \text{ m s}^{-1}$ ), but the winds subsided during morning and evening transition periods. The vertical ( $z$ ) velocity component (Fig. 4) showed a discernible kinematic relation with the along-slope wind intensity and direction. During the daytime uphill flow  $W$  has a positive bias (though the average  $W$  is vanishingly small), while  $W < 0$  during the nocturnal downhill flows of

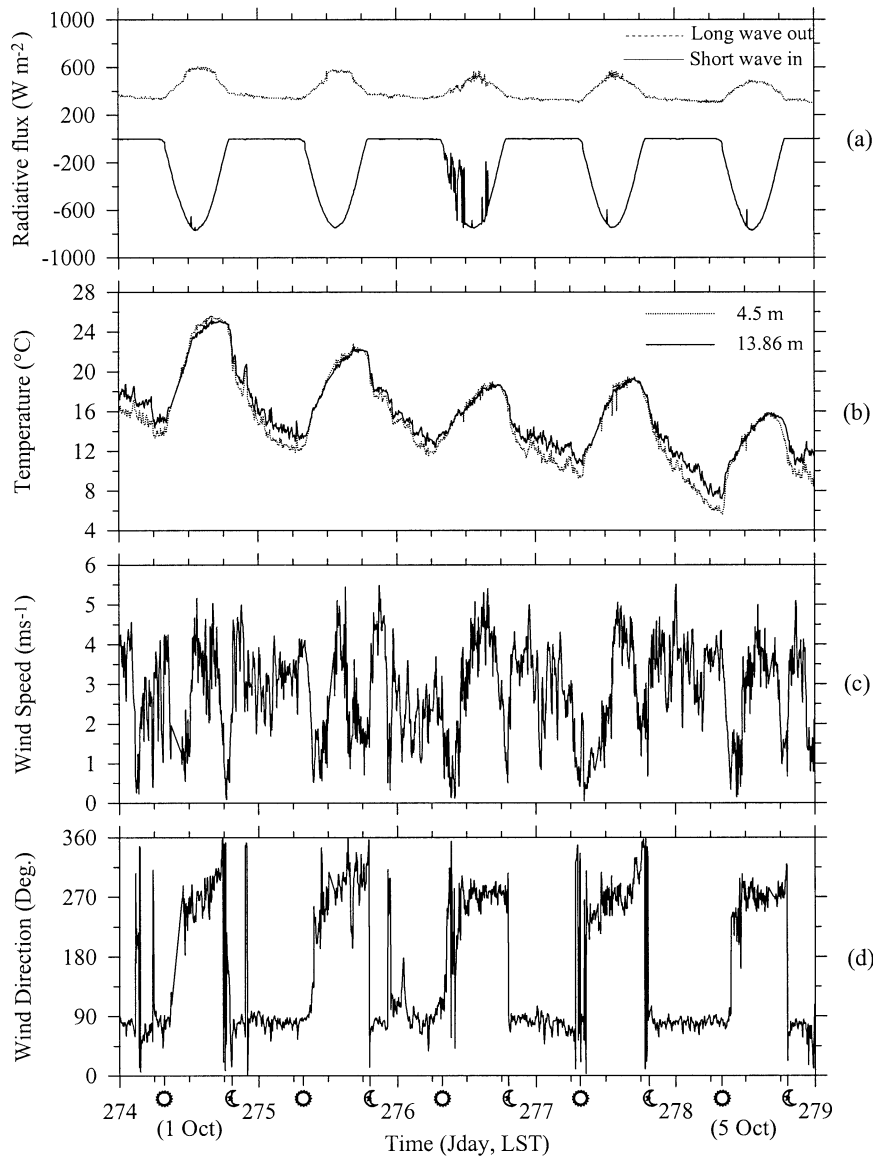


FIG. 3. 5-min time averages of variables during the period 1–5 Oct (Jdays 274–279) of (a) incoming shortwave (solid line) and outgoing longwave (dashed line) radiation, (b) air temperature at 13.86 m (solid line) and 4.5 m (dashed line), (c) wind speed at 13.86 m, and (d) wind direction at 13.86 m. The incoming shortwave radiation is considered negative and outgoing longwave radiation is positive. The symbols the sun (☉) and the crescent moon (☾) indicate the time of sunrise and sunset, respectively.

which the thickness is small enough to register entrainment effects at their edges.

The differences (and some similarities) between the up- and downslope currents are well illustrated by the rms of air temperature  $\sigma_T$  and of the three velocity components  $\sigma_u$ ,  $\sigma_v$ , and  $\sigma_w$  (Fig. 5) as well as the square root of the total vertical flux of horizontal momentum  $[(u'w')^2 + (v'w')^2]^{1/4} \equiv u_{*z}$  and the vertical heat flux  $w'T'$ , calculated using 5-min averaging of data recorded at 13.86 m (Fig. 6). As for their mean counterparts, a daily periodicity was observed for rms velocities, with

higher daytime values than those at night. This is not surprising, given that katabatic winds are stably stratified currents with small vertical exchange coefficients. Conversely, daytime upslope flows are accompanied by convective turbulence, triggered by ground heating, and up- and downdrafts associated with convection lead to higher variability (or gustiness) of wind direction (Fig. 3d).

Similar remarks can be made regarding the daily variation of momentum and sensible heat fluxes (Fig. 6). The latter attained its maximum positive value ( $\sim 0.2^\circ\text{C}$

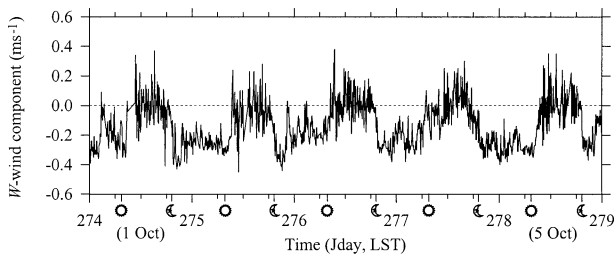


FIG. 4. As in Fig. 3, but for the vertical  $W$  wind component at 13.86 m.

$\text{m s}^{-1}$ , i.e.,  $\sim 200 \text{ W m}^{-2}$ , directed upward) at 1400 LST (Fig. 6b), corresponding to the maximum solar insolation. Because of the decrease of incoming radiation, the sensible heat flux also decreases during the evening, reversing its sign approximately at the sunset. Note that, according to Fig. 6b, the negative sensible heat flux is largest in the early evening ( $\sim -0.01^\circ\text{C m s}^{-1}$ , i.e.,  $\sim -10 \text{ W m}^{-2}$ ) and then decreases slowly throughout the night. During the day, the sensible heat flux normalized by the incoming radiation is  $\sim 0.15\text{--}0.2$  (Fig. 6c), which is roughly equivalent to about half of the radiation divergence ( $\Delta R$ ). At night, the normalized sensible cooling flux is about 3%–5% of the longwave radiation. The momentum fluxes tend to be much larger during the convective period as compared to the stable period where the turbulent shear stresses are suppressed (Fig. 6a).

It is important to note that, as evident from Fig. 5d, the temperature rms did not show the strong diurnal modulation that was characteristic of other turbulent quantities. In fact, with the exception of short time periods of low values during morning and evening transition periods, the temperature rms was approximately the same, irrespective of the hour of the day. As will be discussed later, this behavior can be attributed to the presence of significant gravity wave activity at night and turbulent thermal convection during the day, both of which give rise to significant temperature variances.

Note that the observed nighttime turbulence is rather continuous in time (typically  $\sigma_u \sim \sigma_v \sim 0.3 \text{ m s}^{-1}$ ,  $\sigma_w \sim 0.15 \text{ m s}^{-1}$ ) with some interspersed episodic high variance events. This should be contrasted to typical observations in flat terrain boundary layers where turbulence is highly intermittent, characterized by short bursts separated by nonturbulent periods (Mahrt 1998). Continuous production of turbulent kinetic energy associated with ever present strong wind shears in katabatic winds—near the ground, within the flow, and at the interface between flow and the ambient fluid—can be attributed to these observations. Detained fluid that intrudes into the airshed and entrainment flows into the current also produce high localized shears. Because of the damping effect of the stable stratification, the vertical velocity rms tends to be about one-half of the horizontal velocities.

Finally, it is interesting to note that during the 5 days

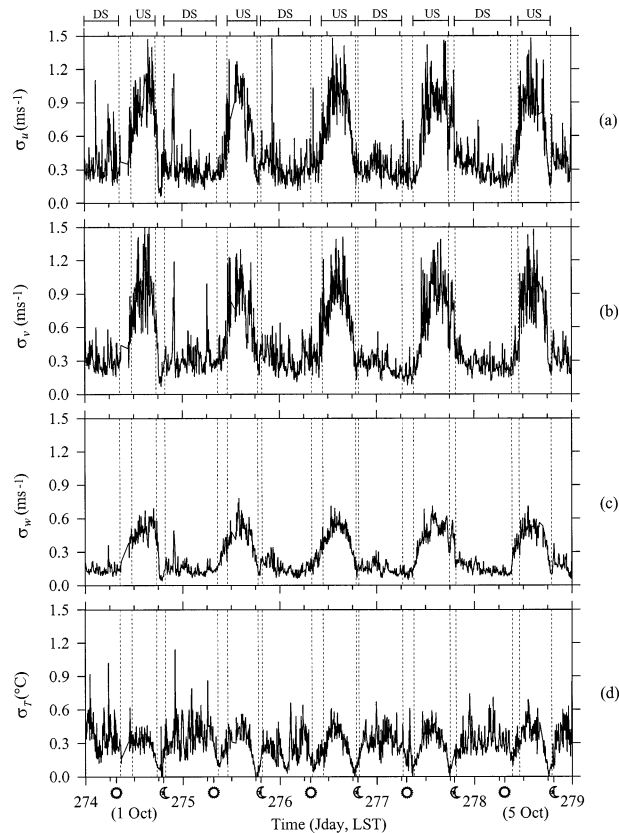


FIG. 5. As in Fig. 3, but for (a)  $\sigma_u$ , (b)  $\sigma_v$ , (c)  $\sigma_w$ , and (d)  $\sigma_T$  at 13.86 m. The time duration of upslope (US) and downslope (DS) winds identified from the analysis of Fig. 3d is indicated at the top.

examined in Figs. 3–6, the mean daily temperature decreased from  $\sim 20^\circ\text{C}$  (Jday 274, 1 Oct) to  $\sim 14^\circ\text{C}$  (Jday 278, 5 Oct), even though the daily thermal excursions remained approximately the same. Neither the mean nor the turbulent quantities were affected by this trend, indicating that slope flow characteristics were essentially dependent on temperature gradients rather than the absolute temperature.

Information on the vertical flow structure can be obtained from the tether sondes measurements. In the following discussion, the flow fields measured during 16–17 October (Jdays 289–290) IOPs will be described. Figures 7a–h show the vertical profiles of both the wind speed and direction and the potential temperature for several tethered balloon soundings. Figure 8 reports 5-min averages of the same variables recorded by the two sonic anemometers during 1800 LST 16 October to 1800 LST 17 October (times marks *a–h* in Fig. 8a correspond to those of vertical soundings depicted in Fig. 7).

Figure 8 suggests that for the day investigated the surface conditions were representative of those observed during the first 5 days in October, that is, daytime upslope and nighttime downslope currents were present (Fig. 3). The evening transition between the up- and downslope flows ended at 1850 LST, when an easterly

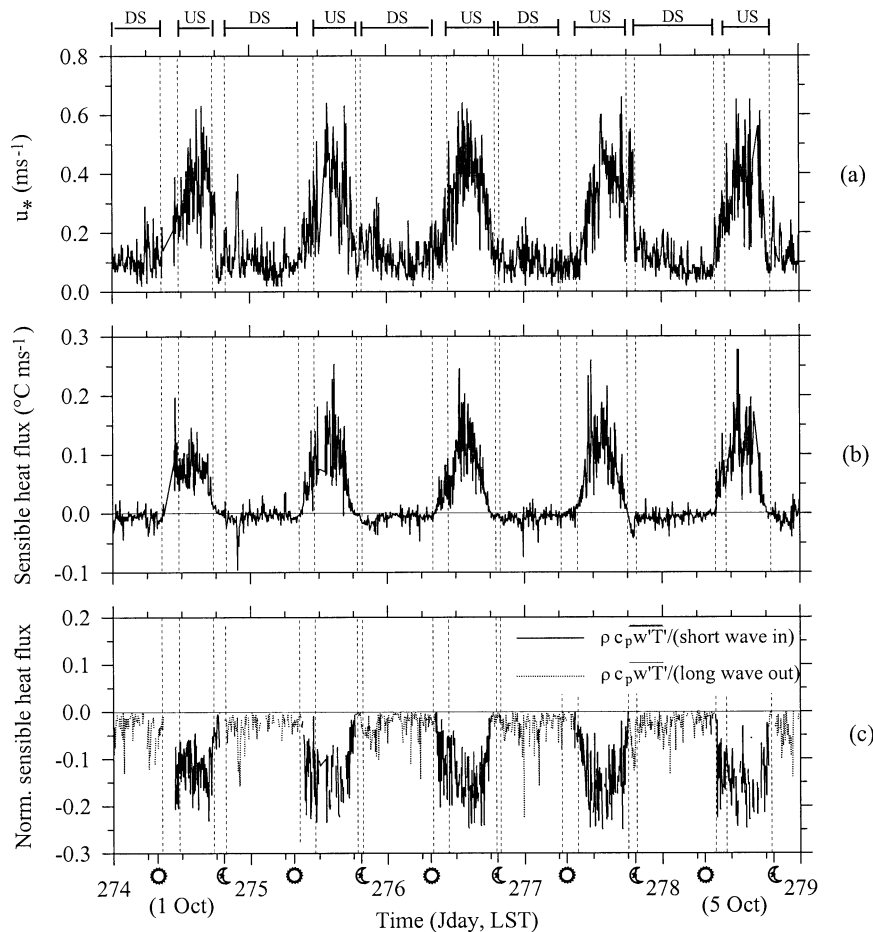


FIG. 6. As in Fig. 5, but for (a)  $u_*$ , (b) sensible heat flux, and (c) sensible heat flux normalized by incoming shortwave (solid line) and outgoing longwave (dashed line) radiation. In (b) and (c), the zero heat flux line is drawn.

wind ( $90^\circ$ ), accompanied by a growth of wind speed and a significant drop in temperature ( $\sim 2^\circ\text{C}$  in 10 min) occurred. Note that the wind direction was approximately the same for both levels during the evening transition. In contrast, the early morning wind rotation from east to west appeared at 13.86 m at 0730 LST, but it occurred only at 0800 LST at 4.5 m (Fig. 8c). Owing to prevailing inertia, a thin residual downslope current may have continued to flow under a newly generated upslope stream for about 30 min! Note the prevailing strong nocturnal stable stratification prior to this event (Fig. 8a) and its abrupt changes by the upslope flow generated at the upper sonic level. The response at the lower level, however, was more gradual. The abrupt reduction of temperature at the 13.86-m level with the directional shift suggests that the upslope flow has been generated at a lower level along the slope and it slides above a thin bottom stable layer until the latter is destroyed. Such disparity of transition at different heights is plausible because, due to the mountain shadowing effect, the morning transition in the lower part of the valley occurs earlier and affects the higher slopes in the

east valley. The flow generated at lower levels moves upslope, meets the existing katabatic flow at higher levels, rises, and flows aloft the katabatic current until the transition on the entire slope is completed. In the presence of an opposing current, the katabatic flow is substantially eroded and hence the residual downslope flow is recorded only at the lower level (see below). This phenomenon, however, was observed only once during the experimental period (i.e., on 16 Oct), and further studies are necessary to investigate its frequency of occurrence. A detailed investigation on flow transitions at ACS will be reported in a future paper.

With the exception of the northwesterly jet recorded at 0623 LST (Fig. 7f), southeasterly/northeasterly winds were generally present above 250 m throughout the night until early morning. Downslope winds with thickness ranging from a few meters to about 50 m occurred near the surface. The analysis of the vertical structure during other IOPs (not reported here) reveals that this was the typical nocturnal behavior at ACS during the VTMX campaign. In addition, the presence of elevated winds with varying direction leads to the hypothesis

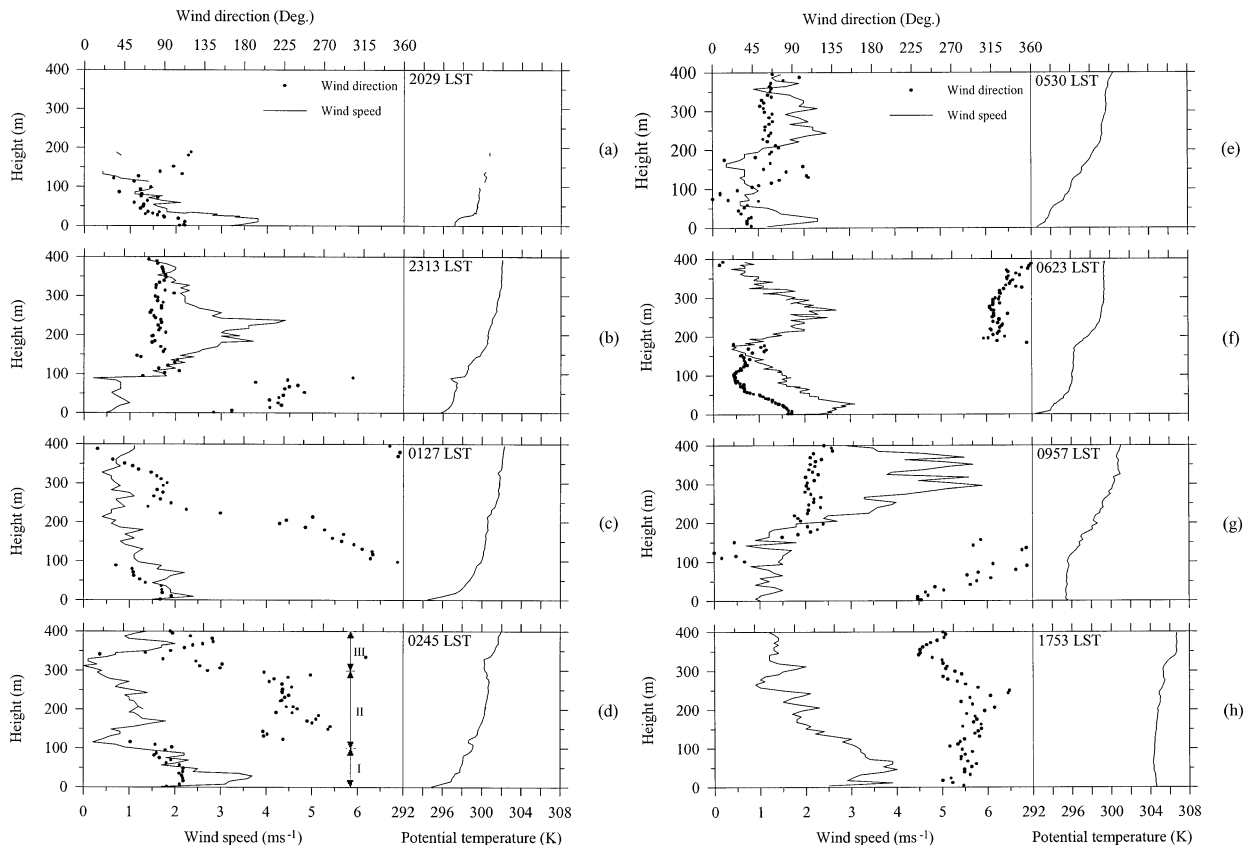


FIG. 7. Vertical profiles of wind speed (solid line), wind direction (full circles), and potential temperature (solid line on the right) for several tethered balloon soundings between the evening of 16 Oct (Jday 289) and the late afternoon of 17 Oct (Jday 290). The profiling rate of sondes was  $\sim 0.8 \text{ m s}^{-1}$ . The time indicated (LST) corresponds to the balloon launching (a typical launch took about 10 min). The three layers indicated by I–III in (d) are described in the text.

that they are thermally induced flows originating from the mountain range encircling the Salt Lake Valley rather than synoptic winds driven by large-scale pressure gradients that penetrate into the airshed.

Some features of the elevated winds on the slope flows are evident from Fig. 9, where two interesting cases recorded during the late evening (1948 LST, Fig. 9a) and late night (2334 LST, Fig. 9b) of 15 October (Jday 288) are reported. In Fig. 9a, an easterly katabatic flow of thickness  $\sim 100 \text{ m}$  and speed of  $\sim 3.5 \text{ m s}^{-1}$  is topped by a low speed ( $\sim 0.5 \text{ m s}^{-1}$ ) layer that is largely northeasterly (100–300 m), which, in turn, is topped by a largely westerly flow ( $\sim 0.5 \text{ m s}^{-1}$ ). Vertical mixing in the lower layer due to cross flow appears to be weak, as indicated by the strong stable stratification near the ground. The flow situation in Fig. 9b is characterized by a thin ( $\sim 15 \text{ m}$ ) katabatic layer of weak easterly flow ( $\sim 1 \text{ m s}^{-1}$ ) topped by a westerly counterflow ( $\sim 2.5 \text{ m s}^{-1}$ ) of thickness  $\sim 50\text{--}75 \text{ m}$  and then another strong easterly flow ( $\sim 4 \text{ m s}^{-1}$ ). Interfaces between the velocity layers are thin, the shear is strong, and hence substantial vertical mixing is expected between the layers. Such mixing is evident from the smeared nature of the density profile (cf. Fig. 9a). Yet signatures of in-

dividual layers are evident from density profiles, especially from density gradients. Elevated winds are associated with the formation of multilayered structures (Figs. 7c–f), perhaps contributed by the intrusion of winds of disparate densities originating at different slopes into the airshed. Because of weak momentum transfer between these layers under stable conditions, they are essentially uncoupled and slide over each other until a strong turbulent mixing event is generated due to the buildup of shear or modified by another intrusive current. Note that the density variation from one intruding layer to another is smooth due to the propensity of intrusions to propagate at their neutral buoyancy levels and to mixing at the sheared boundaries of the layers.

The event recorded at 0245 LST (Fig. 7d) is a typical example of a multilayer structure. It is possible to recognize three different fluid layers, mainly from the velocity profile and to a lesser extent from the density profiles (see arrows). The lowest (I) katabatic flow is from the east up to a height of 50–100 m, the second (II) is a westerly current in a 100–300-m layer, and the winds in the third layer (III) above 300 m were east-southeasterly. Figures 7 and 9 also indicate that the katabatic flow at ACS is far removed from the idealized

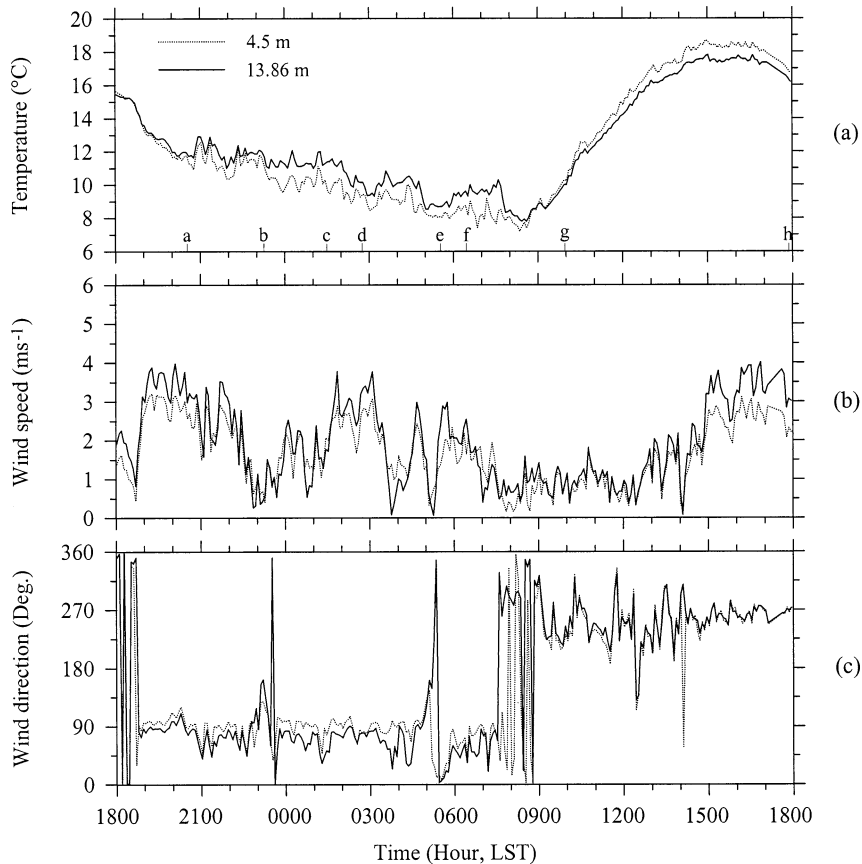


FIG. 8. As in Fig. 3, but for the 24-h period from 1800 LST 16 Oct (Jday 289) to 1800 LST 17 Oct (Jday 290) taken at 13.86 (solid lines) and 4.5 m (dashed lines) of (a) air temperature, (b) wind speed, and (c) wind direction. Letters from *a* to *h* in (a) correspond to the time where each vertical sounding depicted in Fig. 7 was taken.

flow configuration in Fig. 1c. Nonetheless, it is instructive to reckon whether simple formulas such as (1.3) can still provide useful quantitative information on nocturnal flows at ACS. Given that  $B_0$  was not directly measured, the most suitable for comparison is the layer thickness formula (1.3a), based on which the katabatic layer thickness corresponding to the local slope  $\beta = 4^\circ$  (ACS site) is  $h_l \sim 40$  m. For katabatic flows emanating from upstream higher slopes with average slope angle  $\beta_1 = 10.1^\circ$  it is  $h_l \sim 90$  m. On the other hand, using an equivalent slope angle of  $\beta = 5.4^\circ$ , based on the straight line between the site and the top of the ridge, as proposed by Horst and Doran (1986),  $h_l \sim 130$  m. All of these estimates are in reasonable agreement with our observations, which show katabatic layer thickness in the range of 10–100 m. Obviously, the hydraulic adjustment discussed in section 1 and the interaction with other flows in the air basin complicate katabatic flows at ACS. Its prediction, therefore, requires a complete modeling system that takes into account all possible processes.

Figures 7g and 7h show the vertical profiles recorded during the morning transition (0957 LST) and at late

afternoon (1753 LST), respectively. In the former, a thin superadiabatic layer was forming close to the surface by eroding from below the preexisting stable stratified layer. At 1753 LST a convective boundary layer was confined below  $\sim 300$  m, which is the thickness of the existing westerly upslope flow.

#### *b. Turbulence and internal waves in katabatic winds*

As stated in section 1, katabatic flows typify low-level atmospheric stably stratified flows. They are characterized by the ability to sustain internal waves, triggered by such mechanisms as turbulent fluctuations as well as ground-based obstacles and roughness elements. The highest frequency of internal waves is the buoyancy frequency  $N$  given by (1.2), and the stability of such flows can be quantified by the gradient Richardson number (1.4). The virtual potential temperature was utilized in evaluating  $N$ , with ground-level (reference) pressure obtained by a portable barometer every 15 min. Given that the pressure fluctuations are small over the averaging period, the above approximation is reasonable for evaluating the averaged overall Richardson number

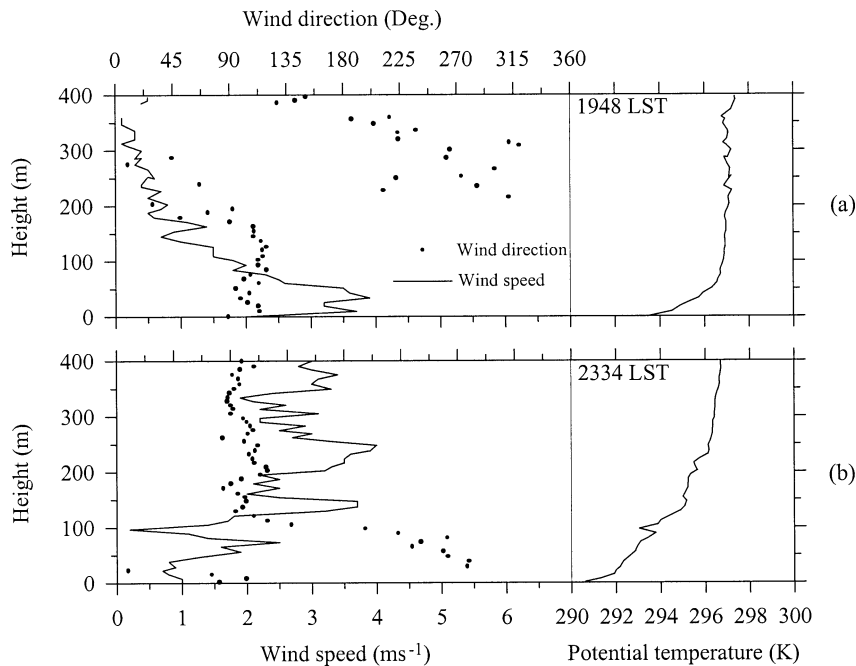


FIG. 9. Typical vertical structure of the flow observed on 15 Oct (Jday 288) during (a) weak winds aloft (velocity  $\sim 0.5 \text{ m s}^{-1}$ , 1948 LST) and (b) sustained elevated winds (velocity  $\sim 3.0 \text{ m s}^{-1}$ , 2334 LST). Solid line show the wind speed and symbols show the wind direction.

$\overline{Ri}_g$ . The 9.36-m vertical distance between the two sonic anemometers was used to calculate gradients. The  $\overline{Ri}_g$  so calculated is assumed to represent the local value, corresponding to the measurement height of turbulent quantities (which are assumed to be dependent on  $\overline{Ri}_g$  only). Typically  $\overline{Ri}_g$  varies with  $z$  and depends on measurement resolution, and hence a question arises with regard to the most appropriate measurement resolution. Given that the vertical resolution was preselected, no checks were made on the dependence of  $\overline{Ri}_g$  on the resolution, which should be borne in mind in interpreting the results. This aspect will be further discussed in section 3c. Figure 10 shows the 5-min averaged  $\overline{Ri}_g$  computed for the five case study days. The dashed lines refer to  $\overline{Ri}_g = 0.25$ , the linear stability limit, and  $\overline{Ri}_g = 1$ , the nonlinear stability boundary. Note the strong modulation of  $\overline{Ri}_g$  over the diurnal cycle. In particular, for the stably stratified period, during which

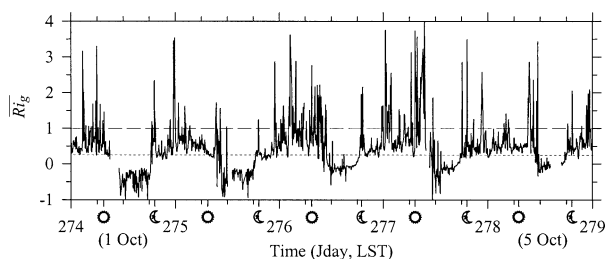


FIG. 10. As in Fig. 3, but the 5-min averaged gradient Richardson number  $\overline{Ri}_g$  is shown. The short dashed line indicates  $Ri = 0.25$  and the long dashed line indicates  $Ri = 1$ .

$\overline{Ri}_g$  assumes positive values, it was in the range 0.2–1.0, except for sporadic bursts with  $\overline{Ri}_g$  exceeding unity.

To investigate the role of gradient Richardson number in flow evolution, time traces of  $\overline{Ri}_g$ , TKE and the temperature variance  $\sigma_T^2$  based on very short averaging periods were analyzed. For example, Figs. 11a,b show a 250-s time interval starting from 0115 LST 5 October (Jday 278), with variables averaged over 1 s. A strong correlation between the TKE and  $\overline{Ri}_g$  is clearly evident: local increase of TKE (maxima) can be construed as corresponding to the local decrease of  $\overline{Ri}_g$  (minima) and vice versa. An increase of TKE is generally evident as the  $\overline{Ri}_g$  falls below a value of about unity, providing support for  $\overline{Ri}_g \approx 1$  threshold; that is, an increase of TKE correlates better with a critical value  $\overline{Ri}_g \approx 1$  rather than  $\overline{Ri}_g \approx 0.25$ . Note, however, that the mean velocity of the flow is  $\sim (-1.75, -0.75) \text{ m s}^{-1}$  (Fig. 11b). Hence, the time traces of Fig. 11a represent the advection of flow containing fluctuations past the probes (i.e., spatial variations), in addition to the time variation of turbulence within the air mass. In the time interval  $0 < t < 140 \text{ s}$ , some periodic oscillations of  $\overline{Ri}_g$  with a period of  $\sim 10\text{--}20 \text{ s}$  were also evident about  $\overline{Ri}_g \approx 1$ , which is the threshold identified by Strang and Fernando (2001a) for most effective mixing and beyond which K–H instabilities disappear. The maintenance of turbulence in the stable layer with a background  $\sigma_w \sim 0.1\text{--}0.3 \text{ m s}^{-1}$  (Fig. 5c) can be attributed, in part, due to the above-mentioned periodic lowering of  $\overline{Ri}_g$  and ensuing instability. At  $t > 140 \text{ s}$ ,  $\overline{Ri}_g$  dropped below 1,

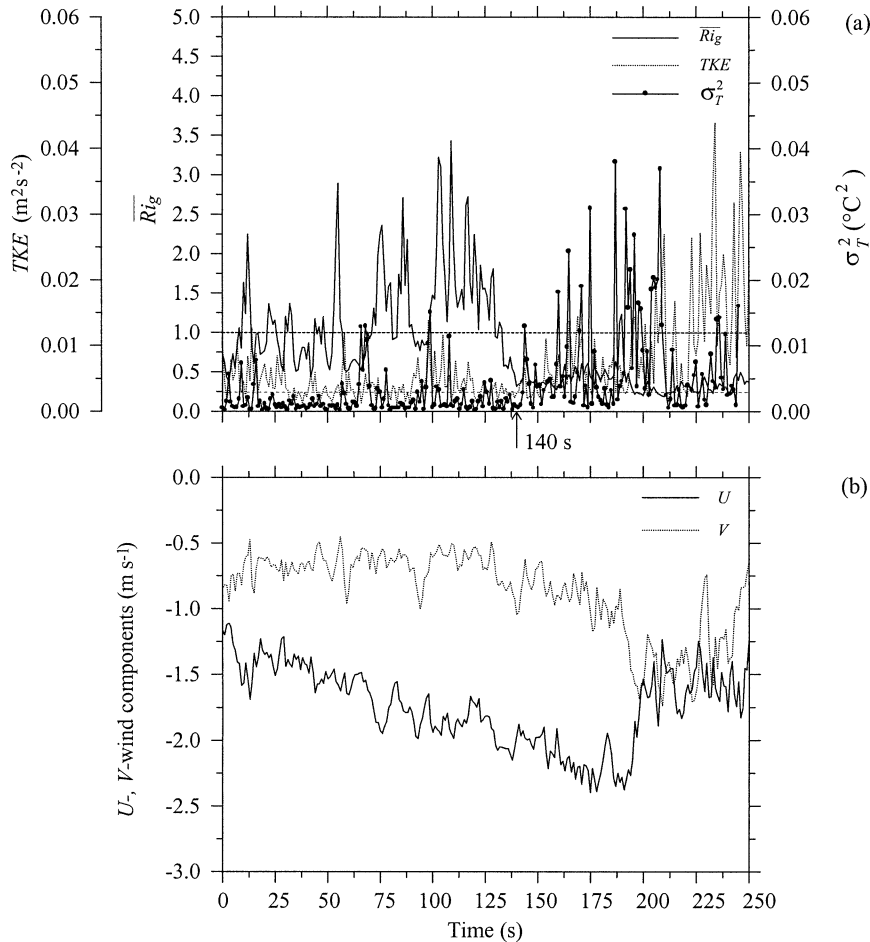


FIG. 11. The 250-s temporal variations measured at 13.86 m starting at 0115 LST 5 Oct (Jday 278). (a)  $\overline{Ri}_g$  (solid line), turbulent kinetic energy TKE (dashed line), and temperature variance  $\sigma_T^2$  (long dashes); (b) horizontal  $U$  (solid line) and  $V$  (dashed line) wind components. Averages over 1 s were used. Limiting values of  $\overline{Ri}_g = 0.25$  and  $\overline{Ri}_g = 1$  are also indicated in (a).

reaching values close to 0.25, and both the TKE and  $\sigma_T^2$  increased significantly.

In Fig. 12, 1-s averaged quantities of a 320-s time trace starting from 2202 LST 1 October (Jday 274) is shown. During this period,  $\overline{Ri}_g < 1$  was maintained (except for sporadic increases), with unstable temperature distributions ( $\overline{Ri}_g < 0$ ) occurring at  $t = 42$  s and  $t = 255$  s followed by an increase of TKE. High frequency  $\overline{Ri}_g$  oscillations with  $\sim 8$  s period followed both events (Fig. 12b). Laboratory observations of Strang and Fernando (2001a) suggest that these oscillations may represent the passage of a series of K–H billows developed upstream. Figures 12a and 12b also show that large  $\overline{Ri}_g$  values that followed K–H billows are due to the decrease of wind shear [ $S^2 = (dU/dz)^2 + (dV/dz)^2$ ] as a result of enhanced momentum transfer, rather than to the lessening of density gradient (or  $N^2$ ) due to enhanced mixing. If the probes continuously record an evolving series of K–H billows, then the above observation implies that during the evolution the momentum

spreads faster than the buoyancy, which is at variance with the concept of equal spreading rates of buoyancy and momentum in high Reynolds number turbulent flows. Conversely, this result can be explained by the tendency of K–H billows to generate and radiate internal waves so as to spread momentum much faster than buoyancy (see section 3d). The increase of  $\overline{Ri}_g$  during the time period  $42 < t < 64$  s leads to a decrease of TKE. The ensuing retardation of the vertical momentum transfer causes shear to rise and hence reduces  $\overline{Ri}_g$  again in  $80 < t < 250$  s. During the latter period, turbulence is maintained without strong overturning activity, pointing to the possibility of turbulent production by shear/turbulence interaction. At  $t = 255$  s, another overturning event follows, leading to enhanced TKE injection to the flow.

Another important aspect is the temperature variance  $\sigma_T^2$ , which, according to Fig. 12c, does not show as significant dependence on  $\overline{Ri}_g$  as TKE. It was noted in section 3a that  $\sigma_T^2$  is not significantly varying during the

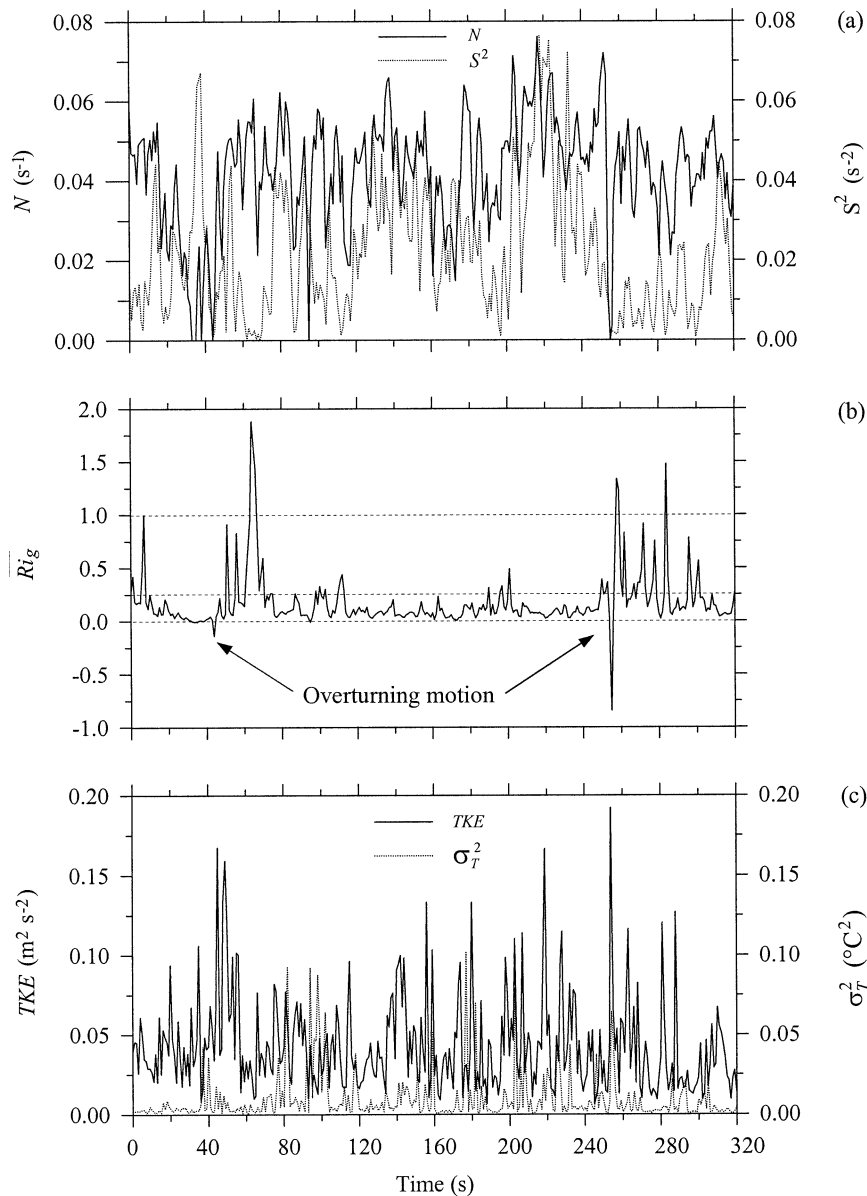


FIG. 12. The 320-s time traces taken at 13.86 m starting at 2202 LST 1 Oct (Jday 274). (a) Buoyancy frequency  $N$  (solid line, in  $\text{rad s}^{-1}$ ) and shear squared  $S^2$  (dashed line), (b)  $\overline{Ri}_g$ , (c) TKE (solid line), and  $\sigma_T^2$  (dashed line) averaged over 1 s.

diurnal cycle (Fig. 5d) either, in contrast to TKE, which subsides at night (Figs. 5a–c and 6a). These observations differ from those made over flat terrain. For example, normalized (by the surface-layer temperature scale  $\theta^* = -w'\theta'/u_{*s}$ ) values of  $\sigma_T^2$  observed in the 1967 Wangara experiments (e.g., Stull 1988) are a factor of 3 less than those observed at ACS at night, albeit their daytime values are comparable. On the other hand, Wangara and ACS dimensionless velocity variances (normalized by  $u_{*s}$ ) are in agreement for both nighttime and daytime cases. Enhanced low-frequency internal wave activity in the katabatic flow may explain large

$\sigma_T^2$  observed in the ACS site. In the Wangara experiments, katabatic flows were absent and the turbulence in the flow was much more intermittent and sporadic, thus lowering averaged  $\sigma_T^2$ .

The possibility of large-amplitude low-frequency internal waves within ACS katabatic flows is exemplified in Fig. 13. Here in Figs. 13a–c the 5-min averages of sensible heat flux, wind speed, and wind direction obtained from the upper sonic during 1800 LST 4 October (Jday 277) to 0900 LST 5 October (Jday 278), respectively, are shown. In spite of the approximate quasi-steadiness of the wind direction after the evening tran-

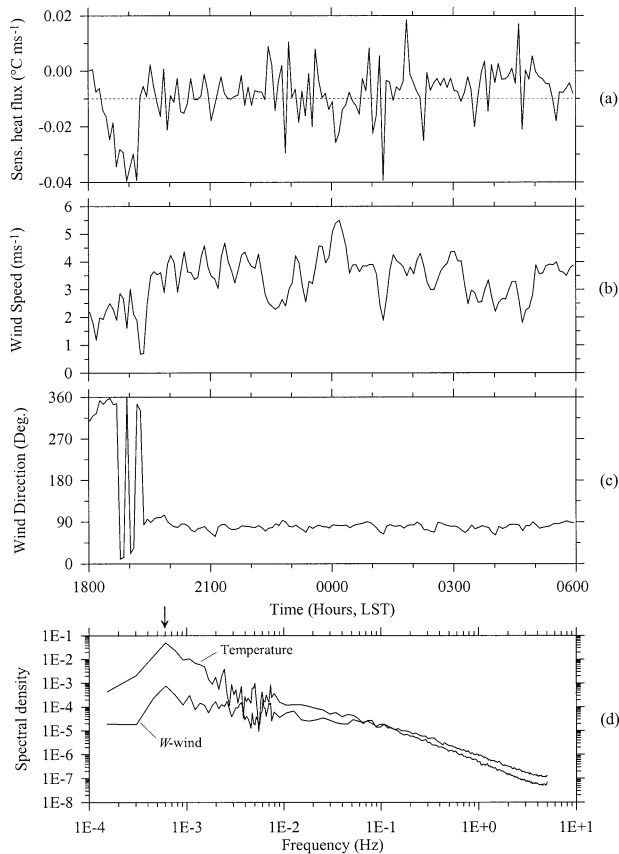


FIG. 13. (a) The 15-h time traces of sensible heat flux, taken at 13.86 m, starting from 1800 LST 4 Oct (Jday 277) to 0600 LST 5 Oct (Jday 278); (b) as in (a) but for the wind speed; (c) as in (a) but for the wind direction; (d) power spectral density of the  $W$  wind component and temperature recorded during the time interval 1920–2230 LST of Jday 277. The arrow corresponds to 28-min period. Averages over 5 min were used in (a), (b), and (c).

sition (Fig. 13c), a distinct series of almost regular oscillations appears to be superimposed on the wind speed and the sensible heat flux (Figs. 13a,b). As evident from the power spectral densities of  $W$  wind and temperature fields calculated for the period 1920–2230 LST and shown in Fig. 13c, these oscillations have a dominant period  $\sim 30$  min; note the peak at the frequency  $6 \times 10^{-4}$  Hz. The flow evolution within one such oscillation is shown in Fig. 14, where time traces of  $\overline{Ri_g}$ , TKE,  $\sigma_z^2$ , and the wind speed averaged over 10 s, starting at 0600 LST 5 October (Jday 278), are plotted for a period of 1800 s. The buoyancy frequency remained approximately uniform ( $N \sim 0.05$  rad s<sup>-1</sup>) during this period. Note the almost periodic oscillations of wind speed and nominally out-of-phase oscillations of  $\overline{Ri_g}$  (or in-phase oscillations of the velocity shear). The period ( $\sim 30$  min) of wind oscillations is much larger than the local buoyancy period  $T_b = 2\pi/N \sim 2$  min, suggesting that these may be low-frequency internal wave oscillations with a nearly vertical wavenumber vector. Noting that the linear wave frequency  $\omega$  is given by  $\omega = N \sin\theta$ ,  $\theta$

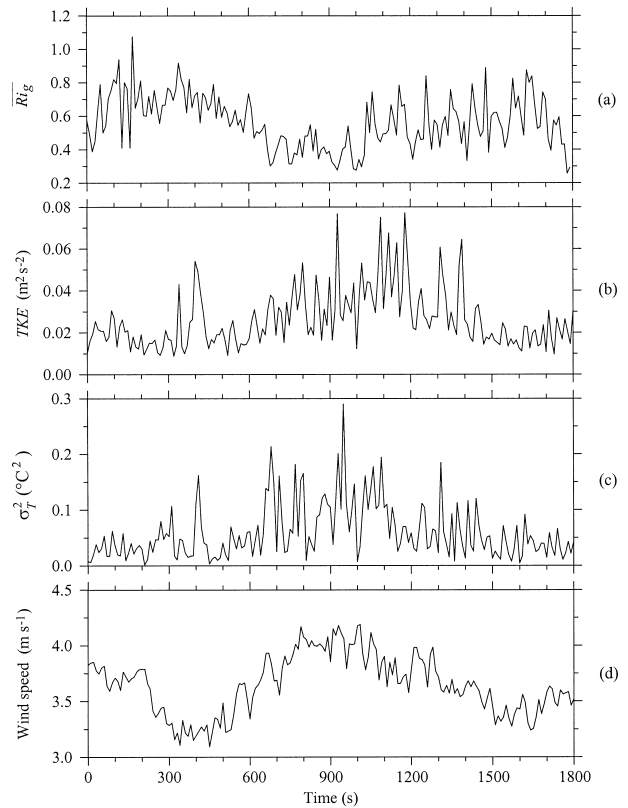


FIG. 14. The 1800-s temporal variation of (a)  $\overline{Ri_g}$ , (b) TKE, (c)  $\sigma_z^2$ , and (d) wind speed at 13.86 m averaged over 10 s from 0600 LST 5 Oct (Jday 278).

being the inclination of wavenumber vector to the vertical, the frequency of such waves with velocity oscillations along the slope (or wavenumber orthogonal to it) can be estimated as  $\omega = N \sin\theta \cong 0.05 \sin 4^\circ \cong 3.5 \times 10^{-3}$  rad s<sup>-1</sup>. The corresponding period  $T_b \cong 30$  min is consistent with the observations [see De Silva and Fernando (1998) for a discussion on low-frequency waves]. This low-frequency behavior and associated elevated  $\sigma_z^2$  were observed during all IOPs at ACS.

The overall flow, therefore, consisted of the mean current, low-frequency ( $\sim 30$  min period) motions sloshing along the slope, internal waves with higher frequencies (but with periods greater than  $T_b = 2\pi/N \sim 2$  min or frequencies below  $8 \times 10^{-3}$  rad s<sup>-1</sup>), and very high frequency small-scale turbulence (Fig. 13d). Low-frequency oscillations have also been noted in the radar data taken during VTMX by D. Parson's group at NCAR (D. Parson 2001, personal communication).

Finally, it is important to note that large-amplitude low-frequency oscillations are a common feature of gravity current flows propagating into stratified fluids. For instance, numerical (Sha et al. 1991) and laboratory (Cenedese et al. 2000) studies of land and sea breezes have shown the existence of wave perturbations after the passage of the sea breeze front. In particular, Sha et al. (1991) found that waves with a time period on the

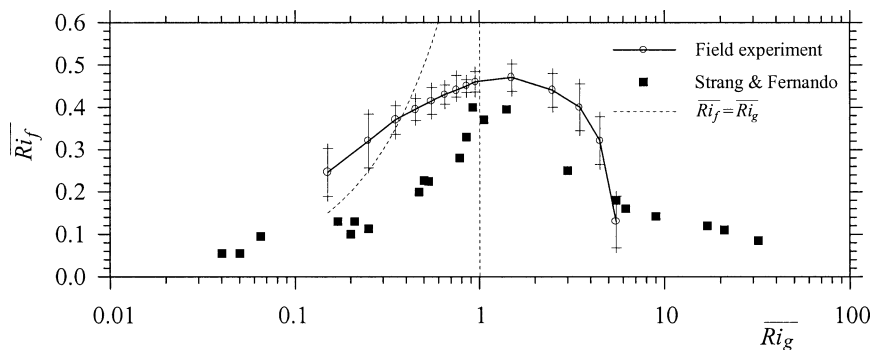


FIG. 15. Flux Richardson number  $\overline{Ri}_f$  (solid line with open circles) as a function of  $\overline{Ri}_g$  based on a dataset taken from 1900 to 0700 LST in the period 1–5 Oct (Jdays 274–278). The error bars refer to the 90% confidence interval of  $\overline{Ri}_f$ . 5-min averages were used. Strang and Fernando's (2001b) laboratory data (full squares) and  $\overline{Ri}_f = \overline{Ri}_g$  (dashed line) are also shown.

order of 35 min were present for 2 h beginning from the passage of the front. Waves of 25–40-min periods were also observed by Donn et al. (1956) in their field investigation of tropical sea breeze circulation. Keon (1982) also reported low-frequency behavior with a period  $\sim 30$  min in the Salt River Valley of Phoenix, Arizona, in regions of slopes and  $N$  values similar to those of ACS.

### c. The flux Richardson number

The flux Richardson number (also known as the mixing efficiency) is defined in terms of the ratio between the buoyancy flux  $\overline{b'w'}$  (the rate of work done by buoyancy forces) and the rate of production of TKE, that is,

$$\overline{Ri}_f = \frac{-\overline{b'w'}}{-\overline{u'u'_j} \frac{\partial U_i}{\partial x_j}} = \frac{-\overline{b'w'}}{\left( -\overline{u'w'} \frac{\partial U}{\partial z} - \overline{v'w'} \frac{\partial V}{\partial z} \right)}, \quad (3.1)$$

and it is extensively used to evaluate eddy diffusivities employed in oceanic (Osborn and Cox 1972) and atmospheric (Mellor and Yamada 1974, 1982) prognostic models. The relation between  $\overline{Ri}_f$  and  $\overline{Ri}_g$  has been studied using laboratory (Linden 1980; McEwan 1983; Rohr and van Atta 1987) and numerical (Caulfield and Peltier 2000) models, but for differing flow configurations. For example, Rohr and van Atta (1987) used a homogeneous stratified shear flow, McEwan (1983) employed breaking internal waves through resonant interactions, and Linden (1980) considered mechanical mixing. Different flow configurations, not surprisingly, have led to widely different  $\overline{Ri}_f$  versus  $\overline{Ri}_g$  relationships, which led Fernando and Hunt (1996) to broadly classify stratified turbulent flows in to several “canonical” classes. Katabatic flows belong to the class of inhomogeneous stratified turbulent shear flows, which also includes other geophysical (e.g., sheared oceanic turbulence in the thermocline, stratospheric jets) as well as laboratory (Strang and Fernando 2001a,b) flows.

For atmospheric flows, it has been customary to use

$z/|L_*|$  to characterize the effects of stratification on turbulence. It can be shown that, based on the Monin–Obukhov similarity theory,  $Ri_f = (z/|L_*|)/\phi_m$ , where  $\phi_m$  is the nondimensional wind shear. Further, for the idealized case of  $\vec{V} = [U(z), 0, 0]$ ,  $Ri_f/Ri_g = K_H/K_M$ , where  $K_H$  and  $K_M$  are the eddy diffusivities of buoyancy and momentum, respectively. Previous work based on flat terrain stable boundary layer data taken in the range  $0 < \overline{Ri}_g < 1$  indicates that  $K_H/K_M$  is approximately constant (e.g., Kaimal and Finnigan 1994; Höglström 1996), but it is instructive to investigate whether this holds true over a broad  $\overline{Ri}_g$  range. Indirect estimates based on oceanic microstructure data show that  $\overline{Ri}_f$  is highly variable (e.g., Strang and Fernando 2001b).

Using the data acquired during 1–5 October (Jdays 274–278) over 1900–0700 LST,  $\overline{Ri}_f$  was evaluated as a function of  $\overline{Ri}_g$ . The upper anemometer was used to evaluate the flux and both anemometers were used to evaluate the shear (the flux measured at the two levels did not differ by more than  $\pm 10\%$ ). A question arises regarding the averaging period, as different averaging times encompass different physical processes. Since main processes of interest were small-scale internal waves and associated turbulence events (which have timescales on the order  $N^{-1} \sim 10$ –20 s; Hunt 1985), an averaging timescale of 5 min was selected. This selection excludes low-frequency internal waves ( $\sim 30$  min) as well as timescales pertinent to large-scale forcing variations (on the order of several hours). Tests with different averaging times showed that  $\overline{Ri}_f$  and  $\overline{Ri}_g$  are insensitive to the averaging time  $T_{av}$  in the range  $30 < T_{av} < 900$  s. Data so evaluated are shown in Fig. 15, with 90% confidence interval indicated by vertical bars. The bins size utilized to calculate  $\overline{Ri}_g$  is one-tenth of the size of the decade in point.

Note that the present results have similarities to those of Strang and Fernando (2001a,b), although the details vary. Both show a maximum  $\overline{Ri}_f \cong 0.4$ –0.5, although  $\overline{Ri}_g$  for this maximum in the field experiment ( $\overline{Ri}_g \sim 1.5$ ) is somewhat larger than that in the laboratory

( $\overline{\text{Ri}}_g \sim 1$ ). Perhaps this discrepancy can be attributed to the vertical resolution used in the present study, that is,  $\Delta z = 9.36$  m. De Silva et al. (1999) reported that  $\overline{\text{Ri}}_g$  measurements are sensitive to  $\Delta z$  as far as  $\Delta z < L_o$ , where  $L_o = (\varepsilon/N^3)^{1/2}$  is the Ozmidov scale based on the TKE dissipation rate  $\varepsilon$ . For the present case,  $\varepsilon$  was evaluated by fitting the Kolmogorov wavenumber ( $k$ ) spectrum  $S(k) = \alpha_k \varepsilon^{2/3} k^{-5/3}$ ,  $\alpha_k \cong 1.6$ , to the inertial subrange discernible in the measured spectrum to obtain  $\varepsilon \approx 1.1 \times 10^{-3} \text{ m}^2 \text{ s}^{-3}$ . By using  $N \sim 0.05 \text{ rad s}^{-1}$ , typical  $L_o$  at the ACS site was found to be less than 3 m, implying that the measured  $\overline{\text{Ri}}_g$  may have some dependence on the measurement resolution. Since De Silva et al. (1999) showed that  $\overline{\text{Ri}}_g$  increases slowly with  $\Delta z$  for  $L_o < \Delta z$ , our calculations might have overestimated the “local”  $\overline{\text{Ri}}_g$ . For Strang and Fernando’s (2001a) data,  $L_o = 0.4\text{--}3.2$  cm and  $\Delta z \sim 0.25$  cm.

Finally, it is important to emphasize that Mellor and Yamada’s (1982) closure model commonly used in geophysical flows employs a constant  $\overline{\text{Ri}}_f$  beyond  $\overline{\text{Ri}}_g = 1$ , which cannot be confirmed by our measurements. Furthermore, it is often assumed that, for  $\overline{\text{Ri}}_g \leq 1$ ,  $K_H/K_M$  is a constant and thus  $\overline{\text{Ri}}_f \propto \overline{\text{Ri}}_g$  (provided the flow is a parallel shear flow). Our data show that  $\overline{\text{Ri}}_f = 0.49\overline{\text{Ri}}_g^{-0.32}$  is more likely for the range  $0.15 < \overline{\text{Ri}}_g < 1$ . A detailed discussion on the dependence of  $\overline{\text{Ri}}_f$  on  $\overline{\text{Ri}}_g$  based on data taken at different sites will be presented in Pardyjak et al. (2002).

#### d. Evaluation of eddy diffusivities

This section deals with eddy diffusivities of momentum

$$K_M = \frac{-\overline{u'w'}}{\partial U/\partial z} \quad (3.2)$$

and heat

$$K_H = \frac{-\overline{w'\theta'}}{d\theta/dz}, \quad (3.3)$$

under stable conditions. Sixty-second averages of data from the same 5 days used for calculations of  $\overline{\text{Ri}}_f$  were used to evaluate  $K_M$  and  $K_H$  in katabatic flows. Figures 16a, 16b, and 16c show, respectively, the dimensional forms of  $K_M$  ( $\text{m}^2 \text{ s}^{-1}$ ),  $K_H$  ( $\text{m}^2 \text{ s}^{-1}$ ), and their ratio  $K_H/K_M$  as a function of  $\overline{\text{Ri}}_g$  (the bin size is the same as in Fig. 15). Empirical best fits to the data show the following relations:

$$K_M = (0.45)\overline{\text{Ri}}_g^{-0.22} \quad (3.4)$$

for the entire  $\overline{\text{Ri}}_g$  range (solid line in Fig. 16a);

$$K_H = (0.07)\overline{\text{Ri}}_g^{-0.45} \quad (3.5)$$

for  $\overline{\text{Ri}}_g < 1$  (solid line in Fig. 16b); and

$$K_H = 0.07, \quad (3.6)$$

for  $\overline{\text{Ri}}_g > 1$  (dashed line). Note that in the  $\overline{\text{Ri}}_g$  range

investigated both  $K_H$  and  $K_M$  are much larger than their molecular diffusive counterparts ( $k_H = 2 \times 10^{-5}$  and  $k_M = 1.5 \times 10^{-5} \text{ m}^2 \text{ s}^{-1}$ , respectively) indicating the dominance of turbulent transport. As evident from Fig. 16c,  $K_H/K_M$  is approximately unity for  $\overline{\text{Ri}}_g < 0.2$ . (This fact, however, is not well reflected in Fig. 15 in terms of the line  $\overline{\text{Ri}}_f = \overline{\text{Ri}}_g$  because of the importance of the  $-\overline{v'w'}$   $dV/dZ$  term, which invalidates  $\overline{\text{Ri}}_f/\overline{\text{Ri}}_g = K_H/K_M$ .) In this range, the stratification effects are of lesser importance and the heat is carried by turbulent eddies at the same rate as momentum: When  $\overline{\text{Ri}}_g > 0.2$ ,  $K_M$  becomes greater than  $K_H$ , which can be attributed to the increasing influence of buoyancy that facilitates internal gravity wave activity. Internal waves transport momentum, but sustain only little (or the ideal case of linear waves, no) buoyancy fluxes. Figures 16a,b also show that in the range  $1 < \overline{\text{Ri}}_g < 10$  the eddy diffusivities have only a weak dependence on  $\overline{\text{Ri}}_g$ . As stated in section 3c, for  $\overline{\text{Ri}}_g \leq 1$ , a common place assumption is that  $K_H/K_M$  is a constant, but this does not hold true over the extended range of  $\overline{\text{Ri}}_g$  investigated here.

According to Strang and Fernando (2001a), K–H billowing subsides beyond  $\overline{\text{Ri}}_g > 1$  and the dominant mixing mechanism becomes the sporadic breaking of Hölmböe and/or internal waves. The buoyancy fluxes associated with such mechanisms are low and hence a lower  $K_H/K_M$  can be expected. Due to the paucity of very high and low  $\overline{\text{Ri}}_g$  events in the time series, data points for  $\overline{\text{Ri}}_g > 20$  have not been subjected to extensive statistical averaging and hence need to be viewed with circumspection.

Also included in Fig. 16c are the laboratory data of Strang and Fernando (2001b), which are in good agreement with the field data until  $\overline{\text{Ri}}_g \sim 10$ . Their laboratory values of  $K_M$  and  $K_H$  were found to fall to corresponding molecular diffusive values when  $\overline{\text{Ri}}_g > 10$ . Typically,  $(\overline{\text{Ri}}_g)_m$ , the value of  $\overline{\text{Ri}}_g$  at which molecular diffusive effects become important increases with the Peclet number  $\text{Pe} = U_1 h_1/k_H$ , and hence with the Reynolds number  $\text{Re} = U_1 h_1/k_M$  (Noh and Fernando 1993); here  $U_1$  and  $h_1$  are the integral velocity and length scales (section 1). Typical Pe for laboratory (Narimousa et al. 1986) and natural shear flows considered here are  $10^6$  and  $10^7$ , respectively. Since Peclet numbers in atmospheric flows are an order of magnitude larger,  $(\overline{\text{Ri}}_g)_m$  values are also expected to be correspondingly higher.

Attempts were made to express eddy diffusivities in nondimensional form by employing suitable length and velocity scales of nocturnal boundary layer. To this end, the buoyancy scale  $L_b = \sigma_w/N$ , the shear scale  $L_s = \sigma_w/|d\tilde{V}/dz|$ , the nocturnal boundary layer height  $h$ , and the integral length scale  $z$  of eddies at a distance  $z$  from the ground were considered as possible length scales, where  $|d\tilde{V}/dz| = \{(dU/dz)^2 + (dV/dz)^2\}^{1/2}$  applies near the ground. Typical values at ACS over the nocturnal period are  $|d\tilde{V}/dz| \sim 0.1 \text{ s}^{-1}$ ,  $\sigma_w \sim 0.2 \text{ m s}^{-1}$ , and  $N \sim 0.05 \text{ rad s}^{-1}$ . Hence, the buoyancy and shear scales are  $L_b$

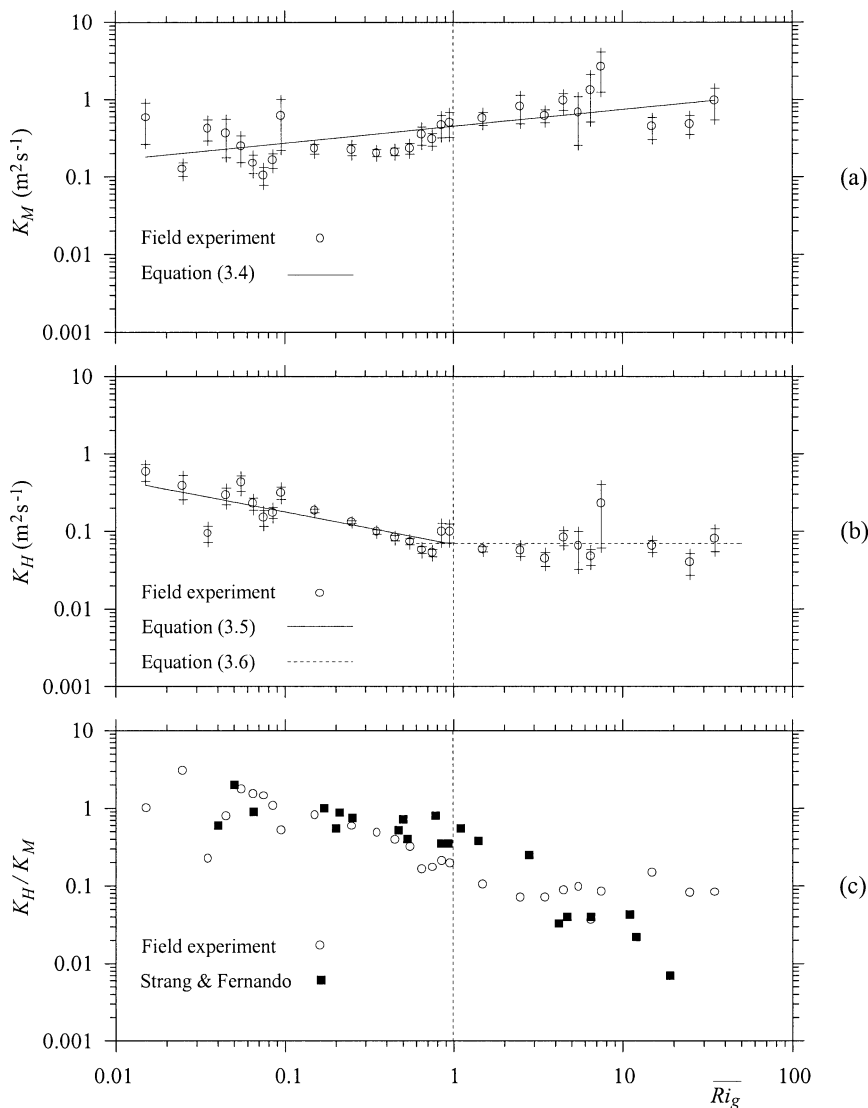


FIG. 16. (a) Dimensional form of the eddy diffusivity of momentum  $K_M$  as a function of  $\overline{Ri}_g$ . The solid line indicates the empirical fit (3.4). (b) Dimensional form of the eddy diffusivity of heat  $K_H$  as a function of  $\overline{Ri}_g$ . The solid line and the dashed line indicate the empirical fits (3.5) and (3.6), respectively. (c) Ratio of the eddy diffusivities  $K_H/K_M$  as a function of  $\overline{Ri}_g$ . The full squares indicate the ratio obtained by Strang and Fernando (2001b). Field data are based on a dataset taken from 1900 to 0700 LST in the period 1–5 Oct (Jdays 274–278). Averages over 60 s were used. The error bars in (a) and (b) refer to the 90% confidence interval of the calculated quantity.

$\cong 4$  m and  $L_s \cong 2$  m, respectively, while  $h \sim 50$  m and  $z = 13.86$  m. The smallest of all scales (i.e., the shear scale  $L_s$ ) is expected to have the dominant contribution to TKE dissipation. In addition, the relevant Monin–Obukhov scale  $L_* = -\theta u_*^3 / (\kappa g w' \theta')$  is of the order of 7 m ( $u_* \sim 0.1$  m s $^{-1}$ ,  $\theta \sim 288$  K, and  $w' \theta' \sim -0.01$  K m s $^{-1}$ ), and hence, the flux measurements taken at  $z = 13.86$  m ( $>L_*$ ) are expected to be governed by the local rather than wall (e.g.,  $u_*$ ) variables. Taking  $\sigma_w$  and  $L_s$  as local velocity and length scales, respectively, a plausible scaling for both eddy coefficients is  $\sigma_w L_s$ , or equivalently  $\sigma_w^2 / |d\bar{V}/dz|$ . The eddy diffusivi-

ties  $K_M$  and  $K_H$  so normalized are shown as a function of  $\overline{Ri}_g$  in Figs. 17a,b. The normalization has arranged the data of Figs. 16a,b to a more regular variation, with normalized  $K_M$  being approximately a constant and normalized  $K_H$  a decreasing function of  $\overline{Ri}_g$ . The best fit lines to the data show

$$\frac{K_M}{\sigma_w^2 / |d\bar{V}/dz|} = (0.34) \overline{Ri}_g^{-0.02} \approx 0.34, \quad \text{and} \quad (3.7)$$

$$\frac{K_H}{\sigma_w^2 / |d\bar{V}/dz|} = (0.08) \overline{Ri}_g^{-0.49} \approx (0.08) \overline{Ri}_g^{-0.5}. \quad (3.8)$$

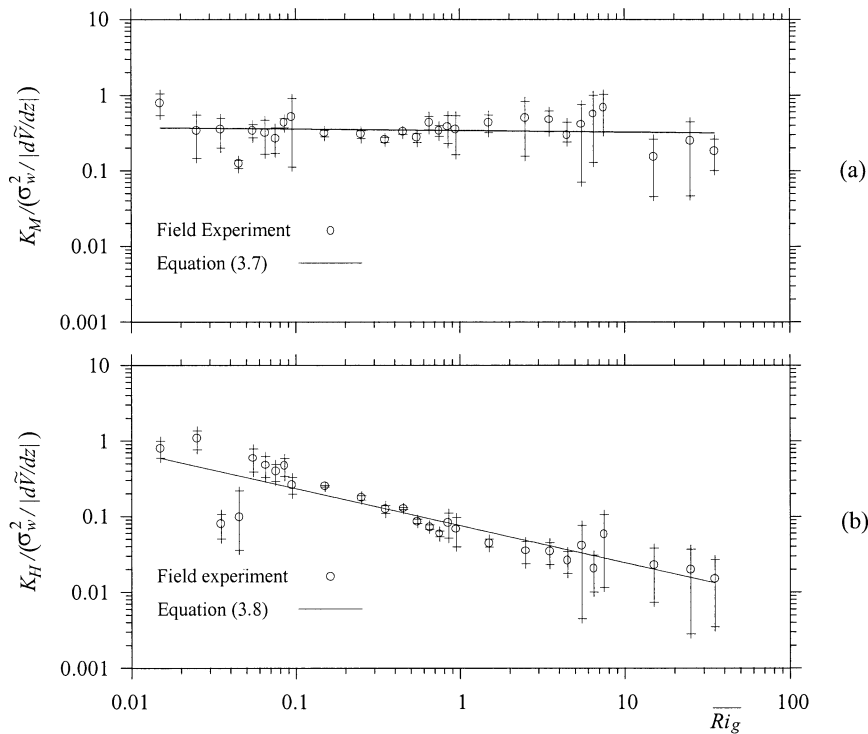


FIG. 17. (a) Nondimensional form of the eddy diffusivity of momentum as a function of  $\overline{Ri}_g$ . The solid line indicates the empirical fit (3.7). (b) Nondimensional form of the eddy diffusivity of heat as a function of  $\overline{Ri}_g$ . The solid line indicates the empirical fit (3.8). Averages over 60 s were used in both cases. The error bars in both the figures refer to the 90% confidence interval of the calculated quantity.

It is interesting that (3.7) and (3.8) reduce to the expressions  $K_M \approx (0.34)\sigma_w^2/|d\tilde{V}/dz|$  and  $K_H \approx (0.08)\sigma_w^2/N$ .

#### 4. Summary and conclusions

Nocturnal atmospheric boundary layer data taken during the Vertical Transport and Mixing Experiment (VTMX), conducted in the Salt Lake City air basin during October 2000, were used to study the nature of nocturnal circulation in a complex terrain airshed. A 14-m tower instrumented with sonic and cup anemometers, thermistors, and radiometers as well as two tethered balloons carrying meteorological sondes and aerosol samplers were used for measurements. The measurement location (identified as ACS) was an approximately uniform eastern slope of the valley with E–W slope angle  $4^\circ$ , covered with grass and small shrubs away from large obstacles. Located several kilometers to the east of the site were the steeper slopes of the Wasatch Mountain range, which can influence katabatic flows at ACS. Our analysis was focused on periods of clear skies and low synoptic winds, wherein the local thermal circulation dominates the basin. Since the slope flows are primarily driven by diurnal thermal forcing, micrometeorological variables such as temperature, wind velocities, sensible heat, and momentum fluxes showed nearly periodic behavior for the days studied. The rms of tem-

perature fluctuations (5 min averaged), however, remained nearly constant over the entire diurnal cycle, contributed by thermal convection during the day and low-frequency internal wave activity at night. The nocturnal normalized rms temperature fluctuation was significantly higher at ACS than those in flat terrain boundary layers, which could be attributed to these low-frequency internal waves.

The data clearly illustrated an upslope (anabatic) flow during the day and downslope (katabatic) flow at night, both having magnitudes  $\sim 4 \text{ m s}^{-1}$ . The thickness of the anabatic flow was about 100–500 m. The thickness of the katabatic flow appeared to be decreasing with the increasing speed of headwinds aloft; typical thicknesses varied from 10 to 100 m. The observed thicknesses were in broad agreement with those predicted by an idealized theoretical model.

The morning and evening transitions were characterized by low speed, highly variable winds. Sonic anemometers located at 4.5 and 13.86 m indicated that, in general, the both morning and evening transitions occurred at these two levels simultaneously. On one occasion, however, the morning transition in the lower sonic was delayed by half an hour. This phenomenon may be caused by the generation of upslope flows at lower elevations prior to that of the measurement lo-

cation; such upslope flows can stream over the weakening katabatic current at the measurement location.

Layers of different density and wind speed/direction characterized the vertical structure of the flow. The formation of such layers may occur due to different air masses of disparate densities originating at slopes of different orientation surrounding the air basin. The suppression of turbulence by the stable stratification reduces shear stresses between these layers, thus allowing them to slide one above another at their neutrally buoyant levels. This intensifies shear across the layers and hence generates turbulence whence the averaged local gradient Richardson number ( $\overline{Ri_g}$ ) drops below a critical value ( $\sim 1$ ). The fluctuations of ( $\overline{Ri_g}$ ) were pronounced, often crossing the threshold of turbulence production, thereby maintaining, at least weak, turbulence in the katabatic layer. Also, the level of turbulence was modulated concurrent with the ( $\overline{Ri_g}$ ) variation. Turbulent fluctuations in the katabatic layer spanned a broad spectrum, the most striking feature being the low-frequency oscillations (period  $\sim 30$  min) corresponding to internal wave sloshing along the slope. Buoyancy affected (mostly internal wave) fluctuations with frequency less than the buoyancy frequency ( $N$ ) and high-frequency three-dimensional turbulent fluctuations also contributed to the spectrum [see Gibson (1991) and Riley and Lelong (2000) for descriptions of stratified turbulent flows]. Turbulence of the sloping boundary layer considered here is different from its flat terrain counterpart wherein highly intermittent turbulent patches are sporadically generated and decay rapidly (Mahrt 1998).

The variation of density stratification and shear over the night allowed for the measurement of averaged flux Richardson number (mixing efficiency)  $\overline{Ri_f}$  as a function of the mean gradient Richardson number  $\overline{Ri_g}$ , an important relationship used in geophysical closure models. It was found that the  $\overline{Ri_f}$ – $\overline{Ri_g}$  relationship is insensitive to the averaging time, when 30–900-s averaging periods were employed. The results were in broad agreement with the laboratory water tunnel measurements of Strang and Fernando (2001a,b) conducted in an inhomogeneous stratified shear flow (a mixing layer), wherein  $\overline{Ri_f}$  increased to a maximum of  $\sim 0.4$  at  $\overline{Ri_g} \sim 1$  and then decreased. The eddy diffusivities of momentum and heat were evaluated as a function of  $\overline{Ri_g}$  and were found to be well above their molecular counterparts. A striking behavior was noted when the diffusivities are scaled with the shear length scale and the rms of vertical velocity fluctuations.

*Acknowledgments.* This research was mainly supported by the U.S. Department of Energy, under the auspices of the Atmospheric Sciences Program of the Office of Biological and Environmental Research. MP was supported by a fellowship from the Graduate Assistance in Areas of National Need (GAANN) Program of the Department of Education. National Science Foundation (CTS and ATM Programs) and Army Research

Office (Geosciences) also provided support for research related to complex terrain flows at ASU. Two of us, PM and TK, are grateful to the staff of the EFD Program for their kind and generous support during their visit to ASU.

#### REFERENCES

- Arritt, J., and R. A. Pielke, 1986: Interactions of nocturnal slope flows with ambient winds. *Bound.-Layer Meteor.*, **37**, 183–195.
- Baines, P. G., 2001: Mixing in flows down gentle slopes into stratified environments. *J. Fluid Mech.*, **443**, 237–270.
- Blumen, W., R. Banta, S. P. Burns, D. C. Fritts, R. Newson, G. S. Poulos, and J. Sun, 2001: Turbulence statistics of a Kelvin–Helmholtz billow event observed in the nighttime boundary layer during the CASES-99 field program. *Dyn. Atmos. Oceans*, **34**, 187–204.
- Bossert, J. E., and W. R. Cotton, 1994: Regional-scale flows in mountain terrain. Part I: A numerical and observational comparison. *Mon. Wea. Rev.*, **122**, 1449–1471.
- Briggs, G. A., 1981: Canopy effects on predicted drainage flow characteristics and comparison with observations. Preprints, *Fifth Symp. on Turbulence, Diffusion, and Air Pollution*, Atlanta, GA, Amer. Meteor. Soc., 113–115.
- Caulfield, C. P., and W. R. Peltier, 2000: The anatomy of the mixing transition in homogeneous and stratified free shear layers. *J. Fluid Mech.*, **413**, 1–47.
- Cenedese, A., M. Miozzi, and P. Monti, 2000: A laboratory investigation of land and sea breeze regimes. *Exper. Fluids*, **29**, 291–299.
- Cermak, J. E., 1996: Thermal effects on flow and dispersion over urban areas: Capabilities for prediction by physical modeling. *Atmos. Environ.*, **30** (3), 393–401.
- De Silva, I. P. D., and H. J. S. Fernando, 1998: Experiments on collapsing turbulent regions in stratified fluids. *J. Fluid Mech.*, **358**, 29–60.
- , A. Brandt, L. J. Montenegro, and H. J. S. Fernando, 1999: Gradient Richardson number measurements in a stratified shear layer. *Dyn. Atmos. Oceans*, **30**, 47–63.
- Deardorff, J. W., 1970: Convective velocity and temperature scales for the unstable planetary boundary layer and for Rayleigh convection. *J. Atmos. Sci.*, **27**, 1211–1213.
- , and G. E. Willis, 1987: Turbulence within a baroclinic laboratory mixed layer above a sloping surface. *J. Atmos. Sci.*, **44**, 772–778.
- Donn, W. L., P. L. Miltic, and R. Brilliant, 1956: Gravity waves and the tropical sea breeze. *J. Meteor.*, **13**, 356–361.
- Doran, J. C., and T. W. Horst, 1983: Observations and models of simple nocturnal slope flows. *J. Atmos. Sci.*, **40**, 708–717.
- , —, and C. D. Whiteman, 1990: The development and structure of nocturnal slope winds in a simple valley. *Bound.-Layer Meteor.*, **52**, 41–68.
- , J. D. Fast, and J. Horel, 2002: The VTMX 2000 campaign. *Bull. Amer. Meteor. Soc.*, **83**, 537–551.
- Ellison, T. H., and J. S. Turner, 1959: Turbulent entrainment in stratified flows. *J. Fluid Mech.*, **6**, 423–448.
- Fernando, H. J. S., 1991: Turbulent mixing in stratified fluids. *Annu. Rev. Fluid Mech.*, **23**, 455–493.
- , and J. C. R. Hunt, 1996: Some aspects of turbulence and mixing in stably stratified fluids. *Dyn. Atmos. Oceans*, **23**, 35–62.
- , M. Princevac, J. C. R. Hunt, and E. Paradyjak, 2000: Thermal circulation in complex terrain: A case of urban fluid mechanics. *Fifth International Symposium on Stratified Flows*, Vol. II, G. A. Lawrence, R. Pieters, and N. Yonemitsu, Eds., Department of Civil Engineering, University of British Columbia, 649–654.
- , S. M. Lee, J. Anderson, M. Princevac, E. Paradyjak, and S. Grossman Clarke, 2001: Urban fluid mechanics: Air circulation and contaminant dispersion in cities. *Environ. Fluid Mech.*, **1**, 107–164.

- Garrett, A. J., 1983: A drainage flow prediction with a one-dimensional model including canopy, soil and radiation parameterization. *J. Appl. Meteor.*, **22**, 79–91.
- Gibson, C. H., 1991: Laboratory, numerical and oceanic fossil turbulence in rotating and stratified flows. *J. Geophys. Res.*, **96** (C7), 12 549–12 566.
- Högström, U., 1996: Review of some basic characteristics of the atmospheric surface layer. *Bound.-Layer Meteor.*, **78**, 215–246.
- Hootman, B. W., and W. Blumen, 1983: Analysis of night-time drainage winds in Boulder, Colorado during 1980. *Mon. Wea. Rev.*, **111**, 1052–1061.
- Horst, T. W., and J. C. Doran, 1986: Nocturnal drainage flow on simple slopes. *Bound.-Layer Meteor.*, **34**, 263–286.
- Howard, L. N., 1961: Note on a paper of John W. Miles. *J. Fluid Mech.*, **13**, 258–260.
- Hunt, J. C. R., 1985: Diffusion in the stably stratified atmospheric boundary layer. *J. Climate Appl. Meteor.*, **24**, 1187–1195.
- , J. C. Kaimal, and J. E. Gaynor, 1985: Some observations of turbulence structure in stable layers. *Quart. J. Roy. Meteor. Soc.*, **111**, 793–815.
- Kaimal, J. C., and J. J. Finnigan, 1994: *Atmospheric Boundary Layer Flows: Their Structure and Measurement*. Oxford University Press, 289 pp.
- Keon, T. L., 1982: Recurrent nocturnal temperature rises in the Salt River valley, Arizona. M.A. thesis, Arizona State University, 90 pp.
- Lied, N. T., 1964: Stationary hydraulic jump in a katabatic flow near Davis, Antarctica, 1961. *Aust. Meteor. Mag.*, **47**, 40–51.
- Linden, P. F., 1980: Mixing across a density interface produced by grid turbulence. *J. Fluid Mech.*, **100**, 691–703.
- Mahrt, L., 1982: Momentum balance in gravity flows. *J. Atmos. Sci.*, **39**, 2701–2711.
- , 1990: Relation of slope winds to the ambient flow over gentle terrain. *Bound.-Layer Meteor.*, **53**, 93–102.
- , 1998: Stratified atmospheric boundary layers and breakdown of models. *Theor. Comput. Fluid Dyn.*, **11**, 263–279.
- , D. Vickers, R. Nakamura, M. R. Soler, J. Sun, S. Burns, and D. H. Lenschow, 2001: Shallow drainage flows. *Bound.-Layer Meteor.*, **101**, 243–260.
- Manins, P. C., and B. L. Sawford, 1979a: A model of katabatic winds. *J. Atmos. Sci.*, **36**, 619–630.
- , and —, 1979b: Katabatic winds: A field case study. *Quart. J. Roy. Meteor. Soc.*, **105**, 1011–1025.
- McEwan, A. D., 1983: Internal mixing in stratified fluids. *J. Fluid Mech.*, **128**, 59–80.
- McNider, R. T., and R. A. Pielke, 1981: Diurnal boundary-layer development over sloping terrain. *J. Atmos. Sci.*, **38**, 2198–2212.
- Melas, D., I. C. Ziomas, and C. S. Zerefos, 1995: Boundary layer dynamics in an urban coastal environment under sea breeze conditions. *Atmos. Environ.*, **29**, 3605–3617.
- Mellor, G. L., and T. Yamada, 1974: A hierarchy of turbulence closure models for planetary boundary layers. *J. Atmos. Sci.*, **31**, 1791–1806.
- , and —, 1982: Development of a turbulence closure model for geophysical fluid problems. *Rev. Geophys.*, **20**, 851–875.
- Meroney, R. N., 1990: Fluid dynamics of flow over hills/mountains—Insights obtained through physical modeling. *Atmospheric Processes over Complex Terrain, Meteor. Monogr.*, No. 45, Amer. Meteor. Soc., 145–172.
- Miles, J. W., 1961: On the stability of heterogeneous shear flows. *J. Fluid Mech.*, **10**, 496–508.
- , 1987: Richardson's number revisited. *Proc. Third Int. Symp. on Stratified Flows*, Vol. 1, Pasadena, CA, California Institute of Technology, 1–7.
- Nappo, C. J., 1991: Sporadic breakdown of stability in the PBL over simple and complex terrain. *Bound.-Layer Meteor.*, **54**, 69–87.
- , and S. Rao, 1987: A model study of pure katabatic flows. *Tellus*, **39A**, 61–71.
- Narimousa, S., R. R. Long, and S. A. Kitaigorodskii, 1986: Entrainment due to turbulent shear flow at the interface of a stably stratified fluid. *Tellus*, **38A**, 76–87.
- Nieuwstadt, F. T. M., 1984: The turbulent structure of the stable, nocturnal boundary layer. *J. Atmos. Sci.*, **41**, 2202–2216.
- Noh, Y., and H. J. S. Fernando, 1993: The influence of molecular diffusion on the deepening of the mixed layer. *Dyn. Atmos. Oceans*, **17**, 187–215.
- Osborn, T. R., and C. S. Cox, 1972: Oceanic fine structure. *Geophys. Fluid Dyn.*, **3**, 321–345.
- Papadopoulos, K. H., and C. G. Helmis, 1999: Evening and morning transition of katabatic flows. *Bound.-Layer Meteor.*, **92**, 195–227.
- Pardyjak, E. R., H. J. S. Fernando, J. Anderson, and N. S. Berman, 1999: Breakdown of complex terrain atmospheric boundary layers. *Bull. Amer. Phys. Soc.*, **44** (8), 135.
- Pearson, H. J., J. S. Puttock, and J. C. R. Hunt, 1983: A statistical model of fluid element motions and vertical diffusion in a homogeneous stratified turbulent flow. *J. Fluid Mech.*, **129**, 219–249.
- Poulos, G. S., and J. E. Bossert, 1995: An observational and prognostic numerical investigation of complex terrain dispersion. *J. Appl. Meteor.*, **34**, 650–669.
- Prandtl, L., 1952: *Essentials of Fluid Dynamics*. Hafner, 452 pp.
- Riley, J. J., and M. P. Lelong, 2000: Fluid motions in the presence of strong stable stratification. *Annu. Rev. Fluid Mech.*, **32**, 613–657.
- Rohr, J. J., and C. W. van Atta, 1987: Mixing efficiency in stably stratified growing turbulence. *J. Geophys. Res.*, **92**, 5481–5488.
- Scorer, R. S., 1978: *Environmental Aerodynamics*. Ellis Horwood, 488 pp.
- Sha, W., T. Kawamura, and H. Ueda, 1991: A numerical study on sea/land breezes as a gravity current: Kelvin–Helmholtz billows and inland penetration of the sea-breeze front. *J. Atmos. Sci.*, **48**, 1649–1665.
- Simpson, J. E., 1999: *Gravity Currents*. Cambridge University Press, 258 pp.
- Snyder, W. H., L. H. Khurshudyan, I. V. Nekrasov, R. E. Lawson Jr., and R. S. Thompson, 1990: Flow and dispersion of pollutants within two-dimensional valleys. *Atmos. Environ.*, **25A**, 1347–1375.
- Strang, E. J., and H. J. S. Fernando, 2001a: Entrainment and mixing in stratified shear flows. *J. Fluid Mech.*, **428**, 349–386.
- , and —, 2001b: Vertical mixing and transports through a stratified shear layer. *J. Phys. Oceanogr.*, **31**, 2026–2048.
- Stull, R. B., 1988: *An Introduction to Boundary Layer Meteorology*. Kluwer Academic, 666 pp.
- Tripoli, G. J., and W. R. Cotton, 1989: A numerical study of an observed orogenic mesoscale convective system. Part I: Simulated genesis and comparison with observations. *Mon. Wea. Rev.*, **117**, 273–304.
- Whiteman, C. D., 1990: Observations of thermally developed wind systems in mountainous terrain. *Atmospheric Processes over Complex Terrain, Meteor. Monogr.*, No. 45, Amer. Meteor. Soc., 5–42.
- , 2000: *Mountain Meteorology: Fundamentals and Applications*. Oxford University Press, 355 pp.
- Yamada, T., 1981: A numerical simulation of nocturnal drainage flows with strong wind and temperature gradients. *J. Appl. Meteor.*, **28**, 545–554.